

PCCF RI 1101
March 2011



Geant4 simulations of β^+ emitters and prompt
 γ yields for *in beam TOF PET* hadrontherapy
application

Loïc Lestand, Paul Force, Gérard Montarou, Nicoleta Pauna

Clermont Université, Université Blaise Pascal,
CNRS/IN2P3, LPC, BP 10448,
F-63000 CLERMONT-FERRAND

List of Figures

1	<i>Geant4 v 9.2 simulation : dose profile from $^{12}_6\text{C}^{6+}$ at 200 MeV/u in water equivalent material for different densities. Even a small variation in the density induces a significant modification of the range.</i>	13
1.1	<i>Parameters of the potential for different type of EOS.</i>	20
1.2	<i>The nuclear matter equation of state : the density dependence of the energy per particle in nuclear matter at temperature T=0 is displayed for 4 different sets of parameters [J.Aichelin (1993)]</i>	21
2.1	<i>Diagram of the nuclear radiative transition.</i>	29
3.1	<i>QMD package description. The different steps of the QMD package are shown from top to bottom. the choice of the projectile and target configurations, then the initial dynamic phase that finish with a set of excited fragments. the “handler” that deals with all the deexcitation channels and produces at the end a set of stable particles and fragments.</i>	32
3.2	<i>Deexcitation processes implemented in the QMD package of the Geant4 code</i>	36
4.1	<i>β^+ emitter experimental profiles versus depth for 215 MeV/u, 260 MeV/u and 337 MeV/u carbon ions.</i>	43
4.2	<i>β^+ emitter profile versus depth for 215 MeV/u carbon ions. data refers to normalized experimental depth profiles. QMD represents normalized simulated depth profiles using QMD package (v.9.4.b01)</i>	46
4.3	<i>β^+ emitter profile versus depth for 260 MeV/u carbon ions. data refers to normalized experimental depth profiles. QMD represents normalized simulated depth profiles using QMD package (v.9.4.b01)</i>	47
4.4	<i>β^+ emitter profile versus depth for 337 MeV/u carbon ions. data refers to normalized experimental depth profiles. QMD represents normalized simulated depth profiles using QMD package (v.9.4.b01)</i>	48

5.1	<i>Experimental set-up dedicated to the prompt γ depth profiles measurement. (a) Ganil set-up : 95 MeV/u carbon ions on PMMA target. (b) GSI set-up : 310 MeV/u carbon ions on water target.[Foulher et al. (2010)]</i>	52
5.2	<i>Measured versus simulated prompt γ depth profile. (a) Ganil experiment. (b) GSI experiment. In each case Exp refers to the measurements [Foulher et al. (2010)].</i>	53
5.3	<i>Z versus A spectrum of the QMD Geant4 v.9.2 simulated fragments population produced during $^{12}\text{C} - ^{12}\text{C}$ collisions at 75 MeV/u (a) and 200 MeV/u (b)</i>	54
5.4	<i>E^* versus A spectrum of the QMD Geant4 v.9.2 simulated fragments population produced during $^{12}\text{C} - ^{12}\text{C}$ collisions at 75 MeV/u (a) and 200 MeV/u (b)</i>	55
5.5	<i>Simulation of prompt γ energy spectrum in $^{12}\text{C} - ^{12}\text{C}$ collisions at 75 MeV/u</i>	57
5.6	<i>Simulation of prompt γ energy spectrum in $^{12}\text{C} - ^{12}\text{C}$ collisions at 200 MeV/u</i>	57
5.7	<i>First step of the deexcitation. Only Fermi BreakUp and Evaporation are considered.</i>	59
5.8	<i>Second step of the deexcitation chain. Only PhotonEvaporation is considered.</i>	59
5.9	<i>Geant4 v.9.2 simulated prompt γ energy spectrum for $^{12}\text{C} - ^{12}\text{C}$ collisions at 200 MeV/u. The new handler algorithm is used to handle the deexcitation chain</i>	60
5.10	<i>Geant4 v.9.2 simulated prompt γ energy spectrum for $^{12}\text{C} - ^{12}\text{C}$ collisions at 200 MeV/u. The new handler algorithm is used to handle the deexcitation chain</i>	61
5.11	<i>Excitation energy versus A diagram for QMD Geant4 v.9.2 simulated fragments population produced during $^{12}\text{C} - ^{12}\text{C}$ collisions at 75 MeV/u (a) (b) and 200 MeV/u (c) (d). Results are obtained using the two different handler</i>	62
5.12	<i>Total Geant4 v.9.2 simulated γ yields ((a) 75 MeV/u, (b) 200 MeV/u) with the two different handler</i>	63
5.13	<i>Secondary particle Geant4 v.9.2 simulated yield for $^{12}\text{C} - ^{12}\text{C}$ collisions at 75 MeV/u (a) and at 200 MeV/u (b) with the two different handler</i>	64
5.14	<i>Geant4 v.9.2 simulated excitation energy versus A diagram at the end of the whole deexcitation for excited fragments population produced during $^{12}\text{C} - ^{12}\text{C}$ collisions at 75 MeV/u (a) and at 200 MeV/u (b)</i>	64
5.15	<i>Measured versus Geant4 v.9.4.b01 + new handler simulated prompt γ depth profile: 95 MeV/u $^{12}\text{C}^{6+}$ on PMMA target at the GANIL</i>	66
5.16	<i>Measured versus Geant4 v.9.4.b01 + new handler simulated prompt γ depth profile: 95 MeV/u $^{12}\text{C}^{6+}$ on PMMA target at the GANIL</i>	67
5.17	<i>Measured versus simulated prompt γ depth profile : 310 MeV/u $^{12}\text{C}^{6+}$ on water target at the GSI</i>	68

List of Tables

3.1	<i>The different steps of the G4QMDReaction::ApplyYourself method in Geant4</i>	33
3.2	<i>α, β, γ, ρ_0, L and E_{sym} parameters available in Geant4</i>	34
3.3	<i>Total effective potential parameters available in Geant4</i>	34
3.4	<i>Ground state parameters available in Geant4</i>	35
4.1	<i>β^+ emitters yields in PMMA</i>	42
4.2	<i>β^+ emitter yields in PMMA. \mathcal{Y}_1 refers to production rate given by [I.Pshenichnov et al. (2006)] [Parodi (2005)]. \mathcal{Y}_2 refers to production calculated from depth profiles. Simulations were performed using Geant4 v.9.4.b01 using QMD package. $\epsilon_{\mathcal{Y}_1}$ and $\epsilon_{\mathcal{Y}_2}$ are the relative deviations between QMD and \mathcal{Y}_1 and \mathcal{Y}_2 respectively.</i>	44
5.1	<i>Prompt γ spectrum description . Geant4 v.9.2 simulated $^{12}C - ^{12}C$ collisions</i>	56
5.2	<i>Total spectrum obtained with the new handler</i>	61

Contents

Introduction	11
1 Nuclear collisions dynamics	15
1.1 Macroscopic models : general concepts	16
1.2 Microscopic models : Quantum Molecular Dynamics approach	17
1.2.1 Physical concepts	17
1.2.2 Description of the Hamiltonian	18
1.2.3 Time evolution	20
1.2.4 Clustering and deexcitation	22
2 Statistical deexcitation	25
2.1 Physical concepts	26
2.2 The Fermi Break-Up model	26
2.3 The evaporation model	27
2.3.1 Particle evaporation	27
2.3.2 Photon evaporation	28
2.4 Nuclear radiative transitions	28
3 Geant4 implementation	31
3.1 QMD package description	31
3.2 QMD implementation	32
3.2.1 The collision impact parameter	32
3.2.2 Space phase initialazation	33
3.2.3 Time evolution	35
3.2.4 Two body collision and Pauli blockling	35
3.2.5 Clustering	35
3.3 Statistical deexcitation implementation	35
3.3.1 General overview	35
3.3.2 Fermi BreakUp model implementation	37

3.3.3	Evaporation model implementation	37
3.3.3.1	Particles evaporation	37
3.3.3.2	Photon evaporation	38
3.3.4	Photon emission and forced γ emission	39
4	β^+ emitter production	41
4.1	Description of the experimental data	41
4.1.1	Production rates	41
4.1.2	Depth profiles	42
4.2	Total production rates : simulations versus measurements	44
4.3	Depth profiles : simulations versus measurements	45
4.4	Discussion	49
5	Prompt γ yield	51
5.1	Prompt γ depth profile : present status	51
5.2	Excited fragments spectrum	53
5.3	Deexcitation chain	56
5.3.1	G4ExcitationHandler default class	56
5.3.2	New handler algorithm	58
5.4	Simulations vs measurements	65
5.4.1	Preliminaries	65
5.4.2	Ganil experiment	66
5.4.3	GSI experiment	68

Abstract

Hadrontherapy, also called particle therapy, is a new type of cancer treatment using light ions beams, mainly protons and carbon ions. Since the primary ions range is very sensitive regarding the patient positioning, anatomical modifications induced by the treatment or some other parameters, the treatment control is a crucial issue of the dose delivering. PET technique is a good candidate since some β^+ emitters nuclei are induced by nuclear fragmentation of the primary ions. However, PET acquisition during irradiation is largely perturbed by the large amount of prompt particles (mainly γ). The design of PET like detector is relying on accurate Monte Carlo simulations. Simulations are performed using the Geant4 toolkit and are focusing on the β^+ emitters and prompt γ yields. Different nuclear models available in Geant4 were tested. β^+ emitters production rates and spatial distribution are well reproduced using QMD model. When introducing some modifications in the deexcitation part of the code, prompt γ detection yields are also well reproduced by simulations. QMD and modified deexcitation models available in Geant4 are sufficiently accurate to provide simulations dedicated to the design of an *in beam TOF-PET* for the treatment control in carbon therapy.

Keywords : Hadrontherapy, *in beam TOF-PET*, β^+ emitter, prompt γ , QMD, Fermi BreakUp, Evaporation, Geant4.

Introduction

The discovery of the X and γ rays respectively in 1895 by Wilhem Röntgen, and in 1896 by Henri Becquerel, initiate a new field of activity which are ionizing radiation medical applications. Physics of ionizing particles has been widely applied for medical imaging as well as for therapy.

Different strategies are currently used for the cancer treatment : surgery, radiotherapy and chemotherapy. They could be used separately or combined to adjust the best treatment to each patient. Among all the radiotherapy strategies, one can distinguish external radiotherapy by means of photon beams and/or electron beams, from internal radiotherapy currently named brachytherapy. The availability of new radiopharmaceutic products made of new isotopes are now more and more used for medical diagnosis and also for therapeutic purpose. For instance internal targeted radiotherapy (ITR), which consists in irradiation of small disseminated tumour lesions using injected radiopharmaceuticals has been for a long time successfully used for differentiated thyroid carcinoma treatment. New efficient radiopharmaceutical products for tumour targeting become available, making feasible such successful ITR treatment for other endocrine tumours.

The field of external radiotherapy has been deeply developed for the last 20 years. The aim of each improvement is the conformation to the treatment volume to optimize the dose deposition and to improve the healthy tissue sparing. Among all the techniques available today, the most remarkable are Intensity Modulated RadioTherapy (IMRT), stereotactic radiosurgery or Volumetric Modulated Arc Therapy (VMAT).

However, despite all these improvements, some cancers remain incurable by conventional radiotherapy. The first type of cancers is the deep seated tumors in close vicinity to organs at risks (OAR). The main difficulty in this case is the geometrical conformation of the dose deposition ; it requires a very precise ballistic since OAR are very sensitive to a high dose deposition. Otherwise the surrounding OAR could be over irradiated and the treatment would fail. This type of tumours requires the dose deposition to be well segmented.

The second type of incurable cancers comes from radioresistant tumors. The treatment efficiency relies on the fact that after irradiation healthy tissue repair is better than malignant tissue repair. By fractionating the whole treatment, this repair behavior induces a cell survival differential effect. This differential effect is the basis of the treatment effectiveness. In the case of radioresistant tumors this differential effect is unfavorable to healthy tissues. This type of tumors requires a more effective radiotherapy technique.

In the middle of the 40s Robert R. Wilson published an article called : “*Radiological Use of Fast Protons*” [Wilson (1946)]. Point out two arguments of Wilson’s paper :

The proton proceeds through the tissue in very nearly a straight line, and the tissue is ionized at the expense of the energy of the proton until the proton is stopped. The dosage is proportional to the ionization per centimeter of path, or specific ionization, and this varies almost inversely with the energy of the proton. Thus the specific ionization or dose is many times less where the proton enters the tissue at high energy than it is in the last centimeter of the path where the ion is brought to rest.

The way the protons loose their energy in the interacting middle is greatly favorable for the treatment of deep seated tumors in close vicinity of OAR. The second developed argument is :

It is well known that the biological damage depends not only on the number of ions produced in a cell, but also upon the density of ionization. Thus the biological effects near the end of the range will be considerably enhanced due to greater specific ionization, the degree of enhancement depending critically upon the type of cell irradiated.

So the ionizing radiation efficiency depends on the density of ionization which increases at the end of the ion range. So the treatment of radioresistant cells could be achieved by means of ions. Ion therapy or hadrontherapy opens the way to the treatment of deep seated tumors and/or radioresistant cancers.

The *in situ* dose delivery monitoring is a crucial issue of these treatments quality control since ion range and therefore dosimetry is very sensitive to anatomical changes during the whole treatment period as well to the patient positioning and to the stoichiometric calibration of the CT images used as virtual patient for the dosimetric calculations.

Figure 1 illustrates clearly that even a small variation in the density induces significant modifications of the range.

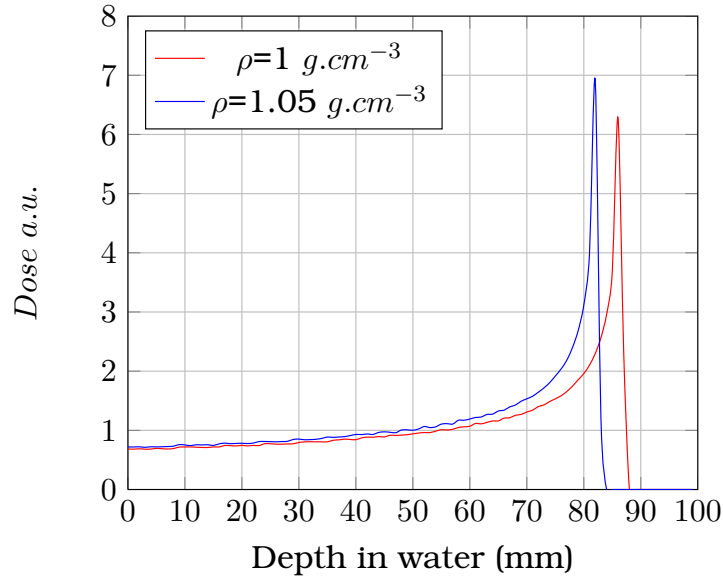


Figure 1: *Geant4 v 9.2 simulation : dose profile from ${}^{12}_6\text{C}^{6+}$ at 200 MeV/u in water equivalent material for different densities. Even a small variation in the density induces a significant modification of the range.*

The dose deposition is induced by the electromagnetic processes. In addition, a lot of secondary particles and fragments are produced through nuclear collisions of the primary ions beam. Among the whole type of fragments, one can distinguish β^+ emitters which are essentially ${}^{10}\text{C}$, ${}^{11}\text{C}$ and ${}^{15}\text{O}$. They are short lived radioisotopes: $T_{10\text{C}} = 20\text{s}$, $T_{11\text{C}} = 20\text{min}$ and $T_{15\text{O}} = 2\text{min}$. During irradiation, the β^+ emitters concentration reach an equilibrium. The induced β^+ activity measurement using PET technique could be one of the possible hadrontherapy treatment control principle.

However, a large amount of γ from nuclear deexcitation are superimposed over the 511 keV annihilation γ . Moreover, those nuclear γ are emitted within few keV and few MeV energy range. Their emission probability is deeply correlated to the primary ions beam temporal structure. Those prompt γ could induce a lot of random coincidences which are considered as background noise regarding the PET technique. To reduce this prompt background noise an acquisition out of ion spill out would be suitable. This technique

was used by Crespo et al [Crespo (2005)] at GSI. The PET acquisition was performed between each 2s spill extraction of the GSI synchrotron beam structure. However, the number of true coincidences is reduced too.

Recent experiments performed at Ganil in Caen with a cyclotron, have demonstrated, given a 80 ns period accelerator signal, that acquisition with a veto applied on the prompt events allows the extraction of the 511 keV annihilation γ from background noise. As a consequence, the conception of a PET device dedicated to the hadrontherapy requires to find a compromise between different parameters such as the beam temporal structure and the detection device performances.

The acquisition of true event will be improved thanks to the design of fast electronics with a high bandwidth and without dead time despite the high rate of prompt γ .

Detectors and dedicated electronics specifications rely on accurate simulations of count rate and bandwidth assessment. Simulations have to reproduce β^+ emitters yields (true signal) and prompt γ yields (background noise).

Sections 1 and 2 will describe the physics of nuclear collisions at hadrontherapy energy range. More specifically, section 1 will consider nuclear dynamics whereas section 2 will be about the statistical deexcitation of fragments.

Section 3 will deal with the implementation in Geant4 of both aspects of the physics of nuclear collisions.

Section 4 will present β^+ emitters yield simulations and comparison with experimental data.

Finally, section 5 will report on the prompt γ yield study. Up to now, Geant4 reproduces the β^+ production rate quite well but overestimates the prompt γ rate up to a factor of 12 [Foulher et al. (2010)].

Chapter 1

Nuclear collisions dynamics

It is commonly assumed that nuclear collisions can be split into three different phases [I.Pshenichnov et al. (2009)].

During the first phase of the reaction, depending on the incident energy of the projectile and the impact parameter, a more or less large amount of nucleons of the projectile and the target (participant nucleons) will interact through binary collisions and/or mean field interactions. The theoretical description of this step is not trivial. At high incident energy (> 500 MeV/u typically), De Broglie wavelength and free mean path of any nucleon involved in the collision is short enough to avoid any quantum mechanics description. For instance, the Pauli exclusion principle is negligible given that the free mean path is very short. During this phase of the collision, it is assumed that nucleons interact mainly through binary collisions which are governed by kinematics parameters such as the minimal distance of interaction $d_{min} = \sqrt{\sigma_{nn}/\pi}$, where σ_{nn} is the nucleon-nucleon interaction cross section. At lower incident energy (< 100 MeV/u typically) quantum mechanics cannot be neglected. Thus nucleons interact only through mean field interactions. At intermediate energies both descriptions are required.

The second stage of the collision is associated with the pre-equilibrium dynamics. During this phase of the reaction, the highly excited system is split into an intermediate set of excited fragments. As the dynamical stage leaves the nuclear matter very excited, energetic nucleon interact through collisions that could lead to particle-hole creation. Then the nuclear matter condensate which means that the nucleons which are close enough to each others are considered belonging to the same fragment [Machner (1979)] while the others are considered as free nucleons.

The third stage of the reaction is the deexcitation of the resulting fragments. During

this stage, all the excited fragments produced in the preequilibrium stage will deexcite via different deexcitation channels. At the end of this stage, all the remaining fragments are supposed to be in ground state.

The complete theoretical description of heavy ions collisions is not an easy task, because of the great number of implied particles. To mitigate this disadvantage, one generally use simplifying assumptions which make possible to define less complex ideal models. These models can be classified summarily in two main categories : the macroscopic and the microscopic models.

1.1 Macroscopic models : general concepts

The hydrodynamic models represent a first example of macroscopic models. They are based on the following assumption: the mean free path of the nucleons, λ , is very small in comparison with the dimensions R of the system. Nuclei are then identified with fluids, and the collision is treated by solving the fluid transport equation, where the nuclear matter equation of state is explicitly involved.

The thermodynamic models are another example of “macroscopic” models. The validity of these models corresponds to the following inequality $R > \lambda > r$ where r is the range of the nuclear forces. This inequality means that the system can be treated like a perfect gas of nucleons in a state of thermodynamic equilibrium. The “fireball” model was one of the first model of this kind : it is considered that all the participating nucleons contained in the intersection volume of the two reacting nucleus (defined by a geometrical cut of the projectile in the target) is in a state of thermodynamic equilibrium. Moreover the impulsion distribution of the nucleons emitted in the the centre of mass of the “fireball” follows the Boltzmann equation of an ideal gas.

The use of statistical thermodynamics concepts to describe the fireball implies the establishment of a chemical equilibrium. That is a chemical balance between the various components of the fireball. This means that the creation rate of the fragments is balanced by their destruction rate until the chemical freezing. The chemical freezing is the beginning of the evaporation phase, where the system is very diluted. At that time of the reaction, the number of interactions between the various components of the fireball is then sufficiently small so that the concentration of the various types of fragments evolve no more.

1.2 Microscopic models : Quantum Molecular Dynamics approach

The Quantum Molecular Dynamics (QMD) is one of the most used microscopic model that could describe heavy ion collision at intermediate energy. It is based on molecular dynamics models with some quantum mechanics considerations such as the Pauli exclusion principle. Such types of models are dealing with the time evolution of any \mathcal{N} body system. The \mathcal{N} individual components of the system mutually interact all together. QMD models take into account binary collisions between nucleons as well as mean field interactions.

1.2.1 Physical concepts

In this section we briefly present the QMD models main concepts.

The first concept is that any nucleon is represented by a gaussian wave packet which depends on two parameters (x_α, p_α) [J.Aichelin (1993)] :

$$\phi_\alpha(x, t) = \left(\frac{2L}{\pi}\right)^{3/4} e^{-L(x-x_\alpha(t))^2} e^{ixp_\alpha(t)} e^{-ip_\alpha^2(t)t/2m} , \forall \alpha \in [1, \dots, A_p + A_t] \quad (1.1)$$

The parameter L, which is related to the extension of the wave packet in phase space, is fixed all along the reaction [Hartnack et al. (1998)].

The second concept is that, neglecting the Pauli exclusion principle, the total wave function is the product of the wave packet of each nucleon :

$$\phi = \prod_{\alpha} \phi_{\alpha}(x, x_{\alpha}, p_{\alpha}, t) , \forall \alpha \in [1, \dots, A_p + A_t]$$

The initial value of the parameters are chosen in such a way that the ensemble of the $A_p + A_t$ nucleons gives an appropriate density distribution as well as an appropriate momentum distribution of the projectile and target nucleus. The evolution of the system is calculated by means of a generalized variational principle starting out from the action.

$$S = \int_{t_1}^{t_2} \mathcal{L}[\phi, \phi^*] dt \quad (1.2)$$

with the Lagrange functional \mathcal{L} :

$$\mathcal{L} = \left(\phi \left| i\hbar \frac{d}{dt} - \mathcal{H} \right| \phi \right) \quad (1.3)$$

The total time derivative includes the derivation with respect to the parameters. The evolution is obtained by the requirement that the action is stationary under the allowed variation of the wave function.

$$\delta S = \delta \int_{t_1}^{t_2} \mathcal{L}[\phi, \phi^*] dt = 0 \quad (1.4)$$

Performing the variation with the total \mathcal{N} body wave function we obtain for each parameter λ an Euler Lagrange equation :

$$\frac{d}{dt} \frac{\partial \mathcal{L}}{\partial \dot{\lambda}} - \frac{\partial \mathcal{L}}{\partial \lambda} \quad (1.5)$$

For the coherent states and an Hamiltonian of the form $\mathcal{H} = \sum_i T_i + \frac{1}{2} \sum_{ij} V_{ij}$ (with T_i and V_{ij} refer to the kinetic and potential energies respectively), the lagrangian and the Euler Lagrange function can be easily calculated :

$$\mathcal{L} = \sum_{\alpha} \left[-\dot{x}_{\alpha} p_{\alpha} + \sum_{\beta} \langle V_{\alpha\beta} \rangle + \frac{3}{8Lm} \right] \quad (1.6)$$

This leads to the two following equations of motion

$$\dot{x}_{\alpha} = \frac{p_{\alpha}}{m} + \nabla p_{\alpha} \sum_{\beta} \langle V_{\alpha\beta} \rangle \quad (1.7)$$

$$\dot{p}_{\alpha} = -\nabla x_{\alpha} \sum_{\beta} \langle V_{\alpha\beta} \rangle \quad (1.8)$$

Thus the variational approach has reduced the \mathcal{N} body Schrödinger equations to a set of $6\mathcal{N}$ differential equations for the parameters which can be solved on present days through computational procedures.

1.2.2 Description of the Hamiltonian

The Hamiltonian of the system has to deal with nuclear interactions which is the crucial ingredient to reach a good description of the nuclear collision dynamics. It can be written as the following equation :

$$\mathcal{H} = \sum_i T_i + \frac{1}{2} \sum_{ij} V_{ij} = \sum_i \frac{p_i^2}{2m} + \frac{1}{2} \sum_{ij} V_{ij} \quad (1.9)$$

During the time evolution the nucleons interact via nuclear interactions (Yukawa potential), charged particles interactions (Coulomb potential) and mean field interactions

(Skyrme potential) [J.Aichelin (1993)].

The potential is commonly written as :

$$V_{ij} = V_{Coul} + V_{Yuk} + V_{loc}^{(2)} + V_{loc}^{(3)} + V_{MDI} \quad (1.10)$$

Let's describe each term :

- The Coulomb potential is V_{Coul} (charged particles interactions)

$$V_{Coul} = \sum_i \sum_{j \neq i} V_{ij}^{Coul} \quad (1.11)$$

with

$$V_{ij}^{Coul} = \frac{e^2}{r_{ij}} \operatorname{erf} \left(\frac{r_{ij}}{2\sqrt{L}} \right) \quad (1.12)$$

- The Yukawa potential is V_{Yuk} (nuclear interactions)

$$V^{Yuk} = t_3 \frac{e^{-|r_1 - r_2|/m}}{|r_1 - r_2|/m} \quad (1.13)$$

- The two body local Skyrme interaction is $V_{loc}^{(2)}$:

$$V_{loc}^{(2)} = t_1 \delta(r_1 - r_2) \quad (1.14)$$

- The three body local Skyrme interaction is $V_{loc}^{(3)}$:

$$V_{loc}^{(3)} = t_2 \delta(r_1 - r_2) \delta(r_1 - r_3) \quad (1.15)$$

- V_{MDI} is an additionnal momentum dependent interaction, which is function of two parameters : t_4 and t_5 . They are determined by a fit to the measured optical potential.

The parameters t_1 and t_2 are determined from the infinite nuclear matter state which is defined by its average binding energy $E/A = -15.75 \text{ MeV}$ and the normal nuclear matter density $\rho = \rho_0 = 0.17 \text{ fm}^{-3}$. As a consequence, the local interaction is a function of the density only.

$$V^{loc}(\alpha, \beta, \gamma) = \alpha \frac{\rho}{\rho_0} + \beta \left(\frac{\rho}{\rho_0} \right)^\gamma \quad (1.16)$$

The parameter γ is introduced to take into account the nuclear matter compressibility.

The choice of those three parameters is depending on the nuclear matter equation state (EOS) [J.Aichelin (1993),J.Aichelin (1991),Polanski (2009)] :

$$\frac{E}{A} = \frac{3p_F^2(\rho)}{10m} + \frac{\alpha}{2} \left(\frac{\rho}{\rho_0} \right) + \frac{\beta}{1+\gamma} \left(\frac{\rho}{\rho_0} \right)^\gamma \quad (1.17)$$

and on the nuclear matter compressibility :

$$\mathcal{K} = 9\rho^2 \left. \frac{\partial^2 E/A}{\partial \rho^2} \right|_{\rho=\rho_0} \quad (1.18)$$

Traditionnaly different sets of values for α , β and γ as well as the nuclear matter compressibility \mathcal{K} are chosen for four different types of nuclear equations of state (EOS) : soft and hard EOS with and without momentum dependent interactions (fixing t_4 and t_5). The corresponding values of the different parameters are summarized in the following table 1.1.

\mathcal{K}	α	β	γ	t_4	t_5	EOS
200 MeV	-356 MeV	303 MeV	7/6			S
380 MeV	-124 MeV	70.5 MeV	2			H
200 MeV	-390 MeV	320 MeV	1.14	1.57 MeV	$5 \cdot 10^{-4} \text{MeV}^{-2}$	SM
380 MeV	-130 MeV	59 MeV	2.09	1.57 MeV	$5 \cdot 10^{-4} \text{MeV}^{-2}$	HM

Figure 1.1: Parameters of the potential for different type of EOS.

All four EOS's give the same ground state binding energy i.e., $E/A=-15.75$ MeV at $\rho = \rho_0$, but they differ drastically at high densities. Here the hard EOS leads to much more compressional energy than the soft EOS at the same density. For infinite nuclear matter at rest the inclusion of the momentum dependent interactions does not change the compressional energy as shown in figure 1.2. We see no difference between the H and HM EOS. Considering heavy ion collisions, the additionnal repulsion due to the initial separation of projectile and target in momentum space shifts the curve for SM and HM interactions to higher energies.

1.2.3 Time evolution

The time evolution of the system in the space phase proceed in two different ways.

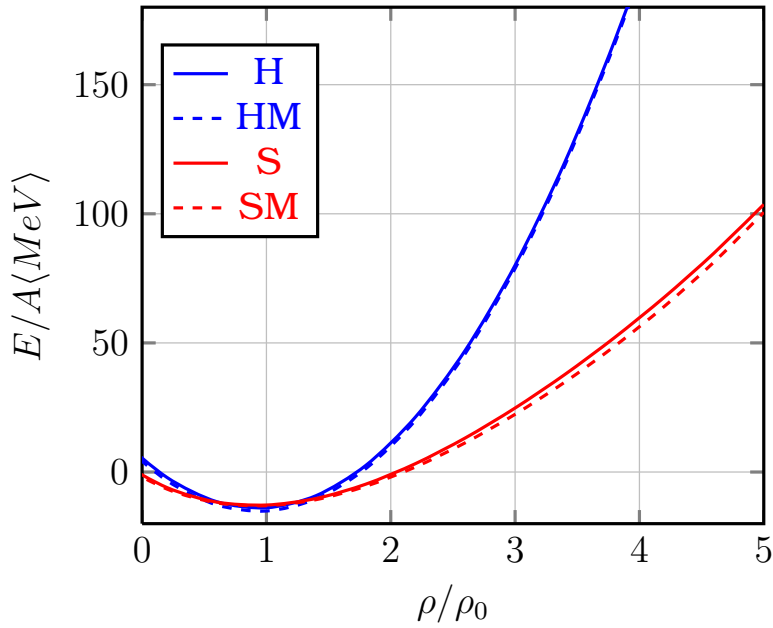


Figure 1.2: The nuclear matter equation of state : the density dependence of the energy per particle in nuclear matter at temperature $T=0$ is displayed for 4 different sets of parameters [J.Aichelin (1993)]

The first one consists of the propagation of the centroid of each gaussian wave packet associated to each nucleon by solving the equations of motion :

$$\begin{cases} \dot{r}_\alpha = \{p_\alpha, H\} \\ \dot{p}_\alpha = \{r_\alpha, H\} \end{cases} \quad (1.19)$$

The second way consists of two body collisions. A pair of nucleon suffers a collision if the distance between the centroids becomes smaller or equal to $d_{min} = \sqrt{\sigma_{nn}/\pi}$, where σ_{nn} is the nucleon-nucleon interaction cross section. Thanks to this binary collision process, it is possible to introduce a Pauli blocking which allows to take the fermionic nature of the nucleons into account. The collision between a pair of nucleon is allowed if the new states in the phase space are not already occupied. Otherwise, the collision is blocked and the nucleons propagate away through the effective potential. The lower the energy, the more collisions are blocked. Thus for very low energy reactions the collisions are not so important. Anyway, QMD remains a phenomenological approach and has to be treated as such.

The differential equations describing the evolution of the centroid of each gaussian wave packet associated to each nucleon are solved by a discretization of the time into small Δt intervals. The integration procedure determines the precision of the calculation. The procedure which is often chosen is the two step Euler method [Polanski (2009)] :

$$first\ step : \begin{cases} r_\alpha \left(n + \frac{1}{2} \right) = r_\alpha(n) + \frac{\Delta t}{2} \left(\frac{p_\alpha(n)}{m} + \nabla V \right) \\ p_\alpha \left(n + \frac{1}{2} \right) = p_\alpha(n) - \frac{\Delta t}{2} \nabla V \end{cases} \quad (1.20)$$

$$second\ step : \begin{cases} r_\alpha(n+1) = r_\alpha(n) + \Delta t \left(\frac{p_\alpha \left(n + \frac{1}{2} \right)}{m} + \nabla V \right) \\ p_\alpha(n+1) = p_\alpha(n) - \Delta t \nabla V \end{cases} \quad (1.21)$$

where $r_\alpha(n)$ or $p_\alpha(n)$ means position or impulsion at time $n\Delta t$. Depending on the initial conditions (incident energy, impact parameter, system size), the time propagation is stopped after 100-200 fm/c.

1.2.4 Clustering and deexcitation

At the end of the propagation procedure, a cluster reasearch is performed [Polanski (2009)]. The nucleons are spread out in the phase space but two nucleons belong to the same cluster if their relative distance in positions space is lower than a certain distance R_{coal} . R_{coal} depends on the fragments formation coalescence time. Its value is different

if the coalescence time is fixed at the chemical freezing time of the reaction (15-30 fm/c [J. Cugnon and Vandermeulen (1982)]), or in the final time of the collision (300 fm/c in our case). Such a theory of coalescence for the fragment formation also required that two nucleons belong to the same cluster if their relative momentum $|\Delta \vec{p}| = |\vec{p}_1 - \vec{p}_2|$ do not exceed a maximal relative momentum p_0 . This parameter was evaluated to 160 MeV/c [Westfall et al. (1984)]. One can approximate R_{coal} value as a function of the coalescence time t through the following relation :

$$R_{coal} = r_{gc} + \frac{p_0}{m} (t - t_{gc}) \quad (1.22)$$

where, m is the mass of the nucleon ($m = 938.3 MeV$), t_{gc} is the time of the chemical freezing and r_{gc} is the chemical freezing corresponding coalescence radius ($r_{gc} = 3$ fm).

For each produced fragment, one determines the mass, total momentum and energy E_{int} , defined as the sum of energies of each nucleon. The total momentum of fragment, P_{frag} is given by the vectorial sum of the momenta of the nucleons which compose this fragment :

$$\vec{P}_{frag} = \sum_i \vec{p}_i \quad (1.23)$$

Each fragment has thus an excitation energy E^* given by

$$E^* = E_{int} - E = \sum_i^N \sqrt{p_i^2 + m^2} - E \quad (1.24)$$

where E is the total energy of the fragment. This energy is calculated starting from the total momentum of the fragment, P_{frag} , and the mass of this fragment estimated by a traditional formula of mass, p_i is the momentum of the i^{th} nucleon of the fragment and m is the nucleon mass.

Some of the fragments produced by coalescence do not exist in ground state, or are too far away from the line of stability of the table of isotopes (too large number of neutrons and protons). These fragments will desintegrate in lighter stable nuclei.

Some other fragments, because of the momenta of the nuclei which compose them, are affected a too large energy which makes them unstable. They will evacuate their excitation energy through emission of photons or light particules.

Each fragment produced by coalescence is thus likely to undergo a process of desintegration or evaporation to form new fragments in their ground state. This define the third step of the whole collision process which is described in the next section.

Chapter 2

Statistical deexcitation

In the previous section, we have briefly described, how excited secondary fragments are produced from a collision of projectile and target ions. In this section we are going to discuss about the models which can be used to deal with the fragments deexcitation.

For excitation energy of about 1 MeV/u, the main deexcitation mechanisms are evaporation of particles and fission for heavier and slightly excited fragments. At these excitation energies, the nuclear density is close to the saturation density $\rho_0 \sim 0.17 \text{ fm}^{-3}$ and the global nuclear properties are well described by the liquid drop model.

For larger excitation energies, $\sim 3 \text{ MeV/u}$, quasi continuous emission of nucleon or light clusters is expected.

At higher excitation energies (5-8 MeV/u) a more explosive deexcitation mechanism is more relevant to describe the equilibrium return [Bondorf et al. (1995)].

There are many models to describe the deexcitation of excited fragments and the emission of intermediate mass fragments (IMF). The statistical multifragmentation model is based on a statistical description of those phenomena. J Bondorf et al define clearly in a Physics Report [Bondorf et al. (1995)] the main idea of the statistical multifragmentation:

the statistical approach which despite of simplicity is very suitable for describing highly excited nuclear systems. Its main idea is that at high excitation energy a very large number of degrees of freedom is involved in the process and the probabilities of different decay channels are mainly determined by statistical weights rather than by the detailed dynamics of the process. This approach makes possible a full description of the highly excited system of hadrons and nucleon clusters in an economic way. It gives wide opportunities to simply imple-

ment many specific features of nuclear systems. But the price for this simplicity is the assumption of statistical equilibrium.

2.1 Physical concepts

Consider now only the mechanisms involved in the fragments deexcitation, and assume that each excited fragment is characterized by a volume \mathcal{V} , an excitation energy E^* , a charge Z_0 and a mass A_0 . Due the excitation energy, the internal pressure is increasing and the volume of the excited fragment will expand. As long as the fragment volume increases, the distance between each nucleon is raising so that the attractive force is not able to maintain any more the cohesion of the fragment. This is followed by the break-up of the fragment into n smaller fragments. For excitation energies considered ($\sim 1 - 10$ MeV/u), the number of decay channels is very large. A statistical description of all possible decay channels is relevant. Each channel is weighted by its probability of occurrence. The probabilities of each fragment deexcitation channel are calculated and randomly chosen.

Depending on the excited system size, different models are available : Fermi BreakUp model for light fragments and Evaporation model for heavier systems.

2.2 The Fermi Break-Up model

For the light clusters ($A \leq 16$) even a small excitation energy is comparable with the binding energy [Bondorf et al. (1987)]. Then, the main break-up mechanism is assumed to be an explosive like mechanism. The probability of each channel can be written as

$$W \propto E_{avai}^{\frac{3n-5}{2}} \quad (2.1)$$

where E_{avai} is total energy available for the set of fragments at the break-up time. This energy is expressed as

$$E_{avai} = E^* + M(A, Z)c^2 - \left(\sum_{i=1}^n m_i c^2 + \epsilon_i \right) - B_{Coul} \quad (2.2)$$

$E^* + M(A, Z)c^2$ refers to the total energy of the fragment in the center of mass (E^* is the excitation energy and $M(A, Z)c^2$ is the mass energy) .

$m_i c^2 + \epsilon_i$ refers to the total energy of each subfragment in the center of mass (ϵ_i is the excitation energy and $m_i c^2$ is the mass energy). B_{Coul} is the Coulomb barrier of the splitting system.

$$B_{Coul} = \frac{3}{5} \frac{e^2}{r_0} \left(1 + \frac{V_{fr}}{V_0} \right)^{-1/3} \left(\frac{Z^2}{A^{1/3}} - \sum_{i=1}^n \frac{Z_i^2}{A_i^{1/3}} \right) \quad (2.3)$$

V_{fr} corresponds to the freeze out volume that may be larger than the volume of the nuclear matter at the saturation point. The final state fragments are supposed to be in their ground or quantized excited state.

As a matter of fact, by forcing the excitation energy of the resulting fragments to be quantized, the whole number of channel is significantly reduced. This is a way to build nuclear level during the deexcitation process.

2.3 The evaporation model

2.3.1 Particle evaporation

For heavier fragments ($A > 16$ typically), the evaporation process through the emission of lighter clusters is assumed to be the main deexcitation mechanism. This model is based on the Weisskopf and Ewing evaporation scheme [Bondorf et al. (1995), Weisskopf and Ewing (1940)]. It is relying on the following equality :

$$P_{p \rightarrow f} = P_{f \rightarrow p} \quad (2.4)$$

The probability of a particle p emits a particle l_c to become a particle f is equal to the probability of a particle f captures the same particle l_c to become the particule p . $P_{f \rightarrow p}$ is proportional to the cross section σ_{inv} of the inverse reaction $(A', Z') + l_c = (A, Z)$. Therefore, the probability that a parent nucleus p with an excitation energy E^* emits a particle l_c in its ground state with kinetic energy ϵ_{kin} is [Weisskopf and Ewing (1940)]:

$$P_{l_c} \propto \sigma_{inv} \frac{\rho_f(E_{max} - \epsilon_{kin})}{\rho_p(E^*)} \quad (2.5)$$

where $\rho_p(E^*)$ is the excited level density of the evaporating nucleus, $\rho_f(E_{max} - \epsilon_{kin})$ that of the daughter (residual) nucleus after emission of a fragment l_c and E_{max} is the maximum energy that can be carried by the ejectile.

The available evaporating channels are : proton channel, neutron channel, deuteron channel, triton channel, ${}^3\text{He}$ channel, α channel. This list can be extended to heavier nuclei, e.g. ${}^{18}\text{O}$, and to photons.

2.3.2 Photon evaporation

The photon emission processes can be added to the deexcitation procedure. Those photons are called statistical photons since their emission is weighted by probabilities. As an exemple, they can come from giant resonances, resulting from nucleon collective motion. The nuclear matter undergoes compression and expansion mechanisms which set in motion the nucleons which lead to collective motions.

The main assumption considers these photons coming from a particular type of giant resonances the so called giant dipole resonances (GDR) [Iljinov et al. (1992)].

The probability to evaporate γ in the energy interval $(\epsilon_\gamma, \epsilon_\gamma + d\epsilon_\gamma)$ is :

$$W_\gamma(\epsilon_\gamma) = \frac{1}{\pi^2 (\hbar c)^3} \sigma_\gamma(\epsilon_\gamma) \frac{\rho(E^* - \epsilon_\gamma)}{\rho(E^*)} \epsilon_\gamma^2 \quad (2.6)$$

where σ_γ is the γ absorption cross section and ρ is the nucleus level density. σ_γ is defined by :

$$\sigma_\gamma = \frac{\sigma_0 \epsilon_\gamma^2 \Gamma_{GDR}^2}{(\epsilon_\gamma^2 - \Gamma_{GDR}^2)^2 + (\epsilon_\gamma \Gamma_{GDR})^2} \quad (2.7)$$

with $\sigma_0 = 2.5A \text{ mb}$, $\Gamma_{GDR} = 0.3E_{GDR}$ and $E_{GDR} = 40.3A^{-1/5} \text{ MeV}$. Then the total probability is calculated as follows

$$W_\gamma = \frac{3}{\pi^2 (\hbar c)^3} \int_0^{E^*} \sigma_\gamma(\epsilon_\gamma) \frac{\rho(E^* - \epsilon_\gamma)}{\rho(E^*)} \epsilon_\gamma^2 d\epsilon_\gamma \quad (2.8)$$

2.4 Nuclear radiative transitions

There is an other photon emission phenomenon which is the nuclear radiative transitions.

Just after the collision dynamical stage, we can imagine that nuclear levels do not exist yet. While the nuclear matter is cooling down, nuclear levels appear. For exemple, particles coming from the Fermi Break Up process are in their ground state or in a quantized excited nuclear state. Therefore, the nuclear transition is a low excitation energy process. So we can distinguish photons coming from giant resonances which are treated as a statistical deexcitation channel and photons coming from nuclear transitions which are treated independently from tabulated data and supposed to occur at the end of the

deexcitation procedure.

Discrete photons production is governed by the nuclear level transition rules. Each excited level is characterized by a mean lifetime τ and the transition probability per unit time is inversely proportional to τ . Moreover, to reproduce the nuclear magic numbers, we need to introduce a strong spin orbit coupling for each nucleon. The existence of this interaction lead to several transition rules since there are energy and angular momenta exchanges for each transition. Those rules are essentially governed by the quantum mechanics and deal with the addition of angular momenta. The figure 2.1 shows schematically the different type of photons which are emitted through nuclear radiative transitions and photon evaporation.

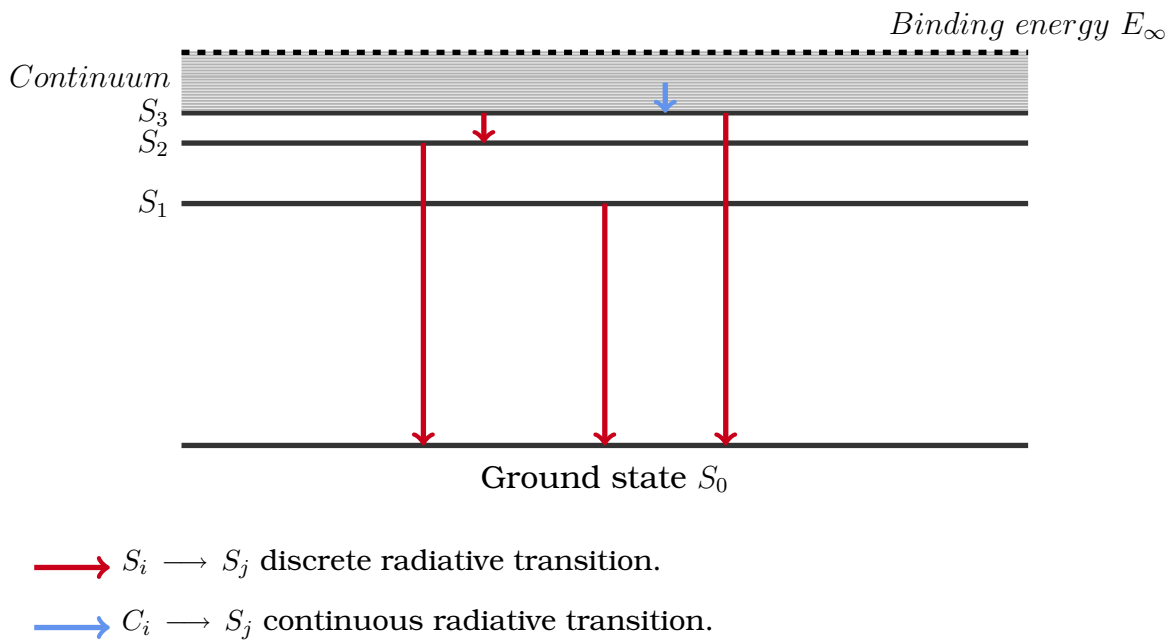


Figure 2.1: Diagram of the nuclear radiative transition.

In conclusion, the Fermi Break-Up model is a good way to treat the main part of fragments. Nuclear transitions model can be used as additional model since excitation energy of the fragments coming from Fermi Break-Up splitting procedure may coincide with nuclear level.

Chapter 3

Geant4 implementation

Geant4 is a Monte Carlo toolkit dedicated to the simulation of the passage of particles through matter. Its domain of application include high energy, nuclear and accelerator physics. It has been extensively used for high energy detector conception and validation. More recently Geant4 is applied for studies in medical and space sciences.

Such a tool has a lot of advantages in comparison with other Monte Carlo code: it is an open source that is also very well documented. The two main reference papers for Geant4 are published in Nuclear Instruments and Methods in Physics Research [[J.Sulkimoah et al. \(2003\)](#)], and IEEE Transactions on Nuclear Science [[J.Allison et al. \(2006\)](#)]. A large community worldwide uses the code and induces so a continuous process of validation. Regular upgrades of the code are distributed (twice a year) through the Geant4 collaboration and its website (<http://geant4.cern.ch/>). There are many courses and tutorial available as well an efficient online user support.

This section is dedicated to the description of the implementation of the physical models for ions collision in the Geant4 toolkit. Hereafter we only consider versions 9.2 till 9.4 of the code.

3.1 QMD package description

One of the most important ingredient for Geant4 simulation is the “physics list”. It defines all the particles and physical processes that will be handled by the code in the user defined application. Geant4 offers a large variety of nuclear processes embedded in several packages. Two different packages are useful for hadrontherapy simulations: Binary Cascade and QMD packages. The term package refers to the association of a collision and deexcitation models. QMD package contains QMD and statistical deexcitation models.

QMD Package
G4QMDReaction:: ApplyYourself(projectile,target)
Excited fragments (A,Z,E*)
G4ExcitationHandler:: BreakItUp(A,Z,E*)
A set of secondary stable fragments

Figure 3.1: QMD package description. The different steps of the QMD package are shown from top to bottom. the choice of the projectile and target configurations, then the initial dynamic phase that finish with a set of excited fragments. the “handler” that deals with all the deexcitation channels and produces at the end a set of stable particles and fragments.

The figure 3.1 describes what are the different phases of the reaction in the QMD package. The input arguments are the projectile and the target. The output arguments are a set of stable fragments. The two main classes involved are **G4QMDReaction** and **G4ExcitationHandler**.

3.2 QMD implementation

The table 3.1 describes the QMD model in Geant4.

3.2.1 The collision impact parameter

The collision is performed given an impact parameter b . The maximum impact parameter b_{max} is calculated from the Shen cross section. The general Shen cross section are given by :

$$\sigma_R = \pi \mathcal{R}^2 \left[1 - \frac{\mathcal{B}}{\mathcal{E}_{CM}} \right] \quad (3.1)$$

where \mathcal{R} is the interaction radius and \mathcal{B} is the nuclear-nuclear interaction barrier. The Shen cross section gives better agreement at energies below 30 MeV/u [Shen et al. (1986)]. The maximum impact parameter is calculated from cross section :

$$b_{max} = \sqrt{\sigma_R / \pi} \quad (3.2)$$

Then, the impact parameter is randomly chosen according to a uniform distribution:

$$b_{reaction} = \sqrt{r} b_{max} \quad (3.3)$$

G4QMDReaction::ApplyYourself(projectile,target)
<ul style="list-style-type: none"> • Maximum Impact parameter b_{max} calculated from Shen Cross Section [Shen et al. (1986)] • Impact parameter of the reaction chosen randomly, $b_{reaction} \in [0, b_{max}]$ • Space phase initialization : <ul style="list-style-type: none"> - G4QMDGroundStateNucleus(G4int z,G4int a) : (r_α, p_α) initialization - G4QMDMeanField meanFiel->SetSystem(projectile+target) : parametrizable mean fiel construction - G4QMDCollision collision->SetMeanField (meanField)
<ul style="list-style-type: none"> • for (G4int i = 0 ; i < 100 fm/c ; i++) meanField->DoPropagation(1 fm/c) Space phase temporal evolution collision->CalKinematicsOfBinaryCollisions(1 fm/c) Binary collisions + Pauli blocking • Clustering <ul style="list-style-type: none"> - $R_{coal} = 4$ fm • A set of excited fragments $\{A,Z,E^*\}$

Table 3.1: *The different steps of the G4QMDReaction::ApplyYourself method in Geant4*

3.2.2 Space phase initialazation

The second step consists in initializing the centroid of each wave packet (r_α, p_α) to build the initial ground state. Moreover, since QMD model is based on \mathcal{N} body interactions through an effective potential, the definition of this effective potential is a crucial ingredient because it rules the dynamics of the system. The total effective potential (cf. section 1) is :

$$V_{ij} = V_{Coul} + V_{Yuk} + V_{loc}^{(2)} + V_{loc}^{(3)} + V_{MDI} \quad (3.4)$$

The Geant4 class which handles the main parameters of the effective potential is **G4QMDParameters**. In the section 1, some parameters were introduced : t_1 and t_2 the two and three body Skyrme interactions, t_3 for the nuclear interaction and t_4 and t_5 for the additionnal momentum dependent interaction.

The parameters handled by the **G4QMDParameters** class for the effective potential definition are called differently. In fact, they are called c_0 , c_3 , c_s and c_l . The two first refer to the two and three body interaction contribution. c_s , refers to the nuclear potential

and c_l refers to the Coulomb interaction. In the Geant4 toolkit, there is no momentum dependent interaction. Each parameter is defined as followed :

$$\begin{aligned}
 c_0 &= \frac{\alpha}{2\rho_0 (4\pi L)^{3/2}} \\
 c_3 &= \frac{\beta(\gamma + 1) (4\pi L)^{3\gamma/2}}{2\rho_0^\gamma} \\
 c_s &= \frac{E_{sym}}{2\rho_0 (4\pi L)^{3/2}} \\
 c_l &= \frac{c_{Coul}}{2}
 \end{aligned} \tag{3.5}$$

Those parameters are in fact function of more physical parameters which are given in the table 3.2.

ρ_0	L	E_{sym}	α	β	γ
0.168 fm ⁻³	2 fm	25 MeV	-219.418 MeV	165.327 MeV	1.33333

Table 3.2: α , β , γ , ρ_0 , L and E_{sym} parameters available in Geant4

The table 3.3 gives an overview of the parameters of the effective potential.

c_0	c_3	c_s	c_l	c_{Coul}
-0.00518291	0.00121007	0.000590529	0.000719883	0.001439767

Table 3.3: Total effective potential parameters available in Geant4

Finally, ground states of the projectile and the target are determined using the four paramters c_{0p} , c_{3p} , c_{sp} , c_{lp} .

$$\begin{aligned}
 c_{0p} &= 2c_0 \\
 c_{3p} &= c_3(\gamma + 1) \\
 c_{sp} &= 2c_s \\
 c_{lp} &= 2c_l
 \end{aligned} \tag{3.6}$$

The table 3.4 sums up the ground state parameters available in Geant4.

c_{0p}	c_{3p}	c_{sp}	c_{lp}
-0.0103658	0.00282349	0.00118106	0.00143977

Table 3.4: Ground state parameters available in Geant4

3.2.3 Time evolution

The propagation procedure is handled by the **G4QMDMeanField::DoPropagation** method and is performed following a two step Euler method. The total evolution time is set to 100 fm/c and the time step is set to 1 fm/c.

3.2.4 Two body collision and Pauli blocking

The collision procedure is managed by the **CalKinematicsOfBinaryCollisions** method from the **G4QMDCollision** class. It is based on the **G4Scatterer** Geant4 class. More precisely the method **theScatterer->Scatter(kt1 ,kt2)** returns a **kinetictrackvector** non dummy if the two nucleons, referred by **kt1** and **kt2** have scattered through elastic process. A Pauli blocking procedure is performed if the elastic collision is allowed.

3.2.5 Clustering

After 100 fm/c, the propagation procedure is stopped. The **G4QMDMeanField:: DoClusterJudgment** method checks if two nucleons are close enough in the phase space. to be considered to belong to the same cluster. Two conditions are required : one distance condition ($r_{min} = 4 fm$) and one momentum condition ($p_{min} = 0.0966 GeV$). p_{min} is deduced from r_{min} according to the Heisenberg uncertainty principle :

$$\frac{r_{min} \times p_{min}}{2} < \hbar c \quad (3.7)$$

The 1/2 multiplication factor is introduced to take the nucleons fermionic nature into account.

3.3 Statistical deexcitation implementation

3.3.1 General overview

The figure 3.2 illustrates the deexcitation processes as implemented in the QMD package of the Geant4 code.

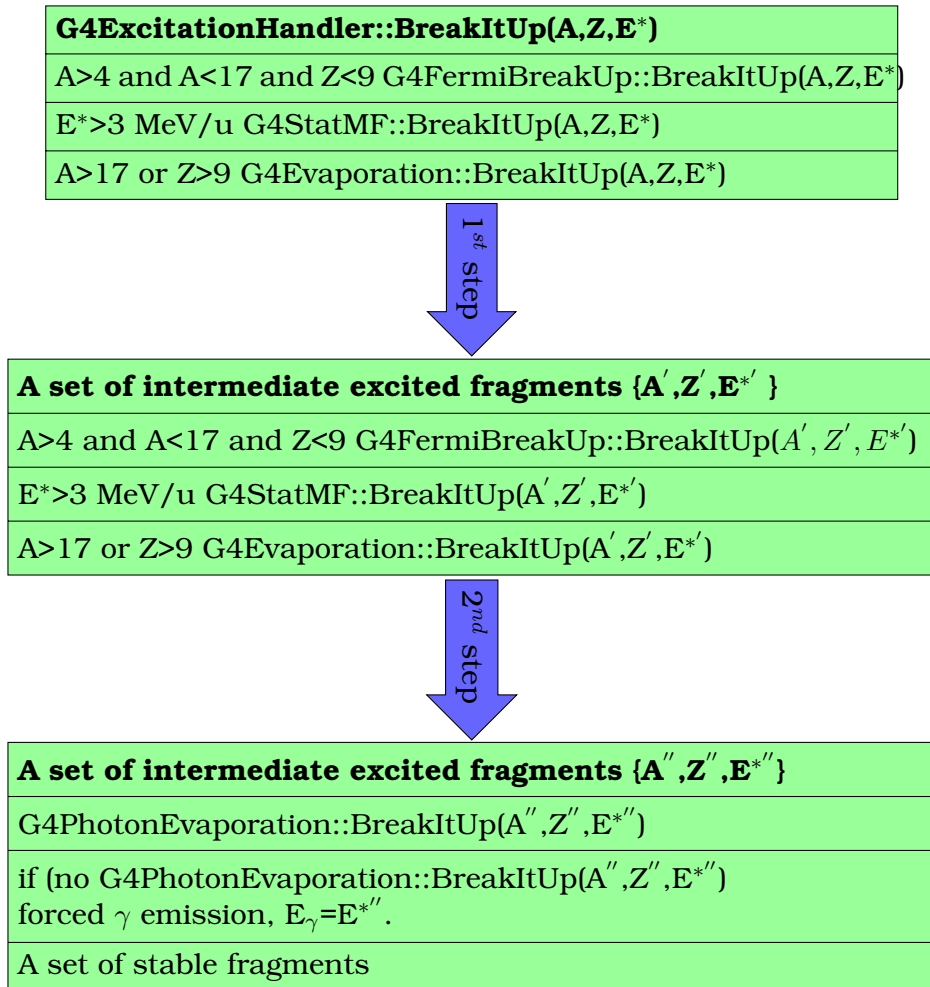


Figure 3.2: Deexcitation processes implemented in the QMD package of the Geant4 code

3.3.2 Fermi BreakUp model implementation

The **G4FermiBreakUp::BreakItUp(A,Z,E*)** method is the main method which handles the Fermi BreakUp deexcitation process. Given an excited fragment, all the break-up channels are evaluated, which means, for each break-up configuration the following quantity is calculated

$$E_{avai} = E + M(A, Z)c^2 - \left(\sum_{i=1}^n m_i c^2 + \epsilon_i \right) - B_{Coul} \quad (3.8)$$

where B_{Coul} is the Coulomb barrier of the splitting system.

$$B_{Coul} = \frac{3}{5} \frac{e^2}{r_0} \left(1 + \frac{V_{fr}}{V_0} \right)^{-1/3} \left(\frac{Z^2}{A^{1/3}} - \sum_{i=1}^n \frac{Z_i^2}{A_i^{1/3}} \right) \quad (3.9)$$

If E_{avai} is strictly positive the break-up probability is calculated. Then each channel probability is sorted and the break-up channel is randomly chosen among all available channels. Note that specific channels are also considered:

- ${}^5_3Li \rightarrow \alpha + p$
- ${}^5_2He \rightarrow \alpha + n$
- ${}^8_4Be \rightarrow \alpha + \alpha$
- ${}^9_4Be \rightarrow \alpha + \alpha + p$

The secondary set of fragments are either in ground state or with some quantized excitation level which allows discrete γ transitions.

We will not describe the **G4StatMF::BreakItUp** since it is dedicated for very excited and heavy fragments. Those fragments are very rare in nuclear collisions involded in the hadrontherapy energy range.

3.3.3 Evaporation model implementation

3.3.3.1 Particles evaporation

The evaporation model used by default in the QMD package is the generalized evaporation model. This model handles emission of fragments heavier than α particles. Here are the particles which could be emitted through an evaporation process : p , n , d , t , 3_2He , 4_2He , and all the stable nuclei till ${}^{28}_{12}Mg$. In addition competitive fission and photon emission channels are considered.

The main method which handles the evaporation process is **BreakItUp(A,Z,E*)** from the class **G4Evaporation**. This method calculates the probability of each channel according to the Weisskopf and Ewing evaporation scheme. For all the channels available, the probabilities are sorted and the channel is randomly chosen using all those probabilities.

Finally it is the **BreakUp(A,Z,E*)** method which proceeds to the deexcitation procedure given an evaporation channel.

Unlike Fermi BreakUp model, fragment excitation energies after evaporation are not quantized since excitation energy is completely determined by the kinetic energy emission of evaporated fragment. This energy is of equal probability distributed between the Coulomb barrier and the maximal kinetic energy that can be carried by fragment. Thus secondary fragment excitation energy is continuously distributed between the emitted fragments.

3.3.3.2 Photon evaporation

If the photon evaporation channel is chosen, the **BreakUp(A,Z,E*)** method from the **G4PhotonEvaporation** class handles the process. The photon evaporation is divided into two components : “discrete” evaporation through nuclear radiative transitions and “continuous” evaporation through the giant dipole resonance.

Discrete levels are tabulated from the first excited level till the last discrete level just before the continuum. If the excitation energy is lower than the last discrete level, referred as the maximum level, the method proceeds to evaporation of a “discrete” photon. Otherwise evaporation of “continuous” photon is performed.

If $E^* > E_{level}^{max}$, the probability to evaporate γ in the energy interval $(\epsilon_\gamma, \epsilon_\gamma + d\epsilon_\gamma)$ is :

$$W_\gamma(\epsilon_\gamma) = \frac{1}{\pi^2 (\hbar c)^3} \sigma_\gamma(\epsilon_\gamma) \frac{\rho(E^* - \epsilon_\gamma)}{\rho(E^*)} \epsilon_\gamma^2 \quad (3.10)$$

σ_γ is the γ absorption cross section and ρ is the nucleus level density. σ_γ is defined :

$$\sigma_\gamma = \frac{\sigma_0 \epsilon_\gamma^2 \Gamma_{GDP}^2}{(\epsilon_\gamma^2 - \Gamma_{GDP}^2)^2 + (\epsilon_\gamma \Gamma_{GDP})^2} \quad (3.11)$$

with $\sigma_0 = 2.5A \text{ mb}$, $\Gamma_{GDR} = 0.3E_{GDP}$ and $E_{GDP} = 40.3A^{-1/5} \text{ MeV}$. Then the total probability

is calculated following the equation :

$$W_\gamma = \frac{3}{\pi^2 (\hbar c)^3} \int_0^{E^*} \sigma_\gamma(\epsilon_\gamma) \frac{\rho(E^* - \epsilon_\gamma)}{\rho(E^*)} \epsilon_\gamma^2 d\epsilon_\gamma \quad (3.12)$$

If “discrete” evaporation is chosen i.e. $E^* < E_{level}^{max}$, nuclear transitions are performed according tabulated data. If the excitation level is lower than $E_{level}^{min}/2$, the excitation is set to 0.

In each case, i.e. “continuous” and “discrete” evaporation, only one photon is evaporated. There is no a cascade.

3.3.4 Photon emission and forced γ emission

The **G4PhotonEvaporation::BreakItUp(A,Z,E*)** method handles the last deexcitation procedure. It acts exactly like **G4PhotonEvaporation::BreakUp(A,Z,E*)** method, however, photon emission is performed while fragments are excited. In case there is no nuclear level found in the nuclear data base, the deexcitation is forced through an artificial γ emission procedure. This procedure emits a γ with an energy equal to the residual excitation energy.

Chapter 4

β^+ emitter production

In the previous sections, the Quantum Molecular Dynamics model and its implementation in the Geant4 toolkit has been described. PET technique is based on the detection of a pair of 511 keV annihilation γ in a narrow time interval (coincidence). Such a technique could be used to the hadrontherapy treatment control with some *in beam* specific adaptations. Nevertheless, the design of such a device requires that one is able to accurately evaluate the β^+ induced count rate. However, PET technique for hadrontherapy application will be used in conditions where, in the spill extraction, a lot of random coincidences coming from the prompt γ are superimposing over the 511 keV coincident γ . This requires to modify the trigger regarding the PET acquisition. Thus, one should also be able to predict such a background noise. Anyway, this section is dealing with the comparison between experimental and Geant4 simulated β^+ emitters production rates. Comparisons are performed in terms of integrated production rates and depth profiles shapes.

4.1 Description of the experimental data

Two different types of measurement are available : production rates and production rates versus depth.

4.1.1 Production rates

The production rate given a β^+ emitters nucleus i is defined as following :

$$\mathcal{Y}_i = \frac{N_i}{N_{ion}} \quad (4.1)$$

where N_i is the number of produced β^+ emitters given N_{ion} primary ions. These experimental data are reported in [Parodi (2005)][I.Pshenichnov et al. (2006)]. One consider

carbon ions interacting with a 300 mm \times 90 mm \times 90 mm PMMA target (PMMA is an equivalent tissue medium). The main resulting β^+ emitters nuclei are ^{10}C ($T_{10\text{C}} = 2\text{ s}$), ^{11}C ($T_{11\text{C}} = 20\text{ min}$) and ^{15}O ($T_{15\text{O}} = 2\text{ min}$). ^{10}C , ^{11}C come from target and projectile fragmentation whereas ^{15}O comes from target fragmentation only. Measurements were performed for three different energies : 212,12 MeV/u, 259.5 MeV/u and 343,46 MeV/u.

212.12 MeV/u	
<i>Nuclei</i>	<i>Experiment</i>
^{10}C	$(8 \pm 3) \times 10^{-3}$
^{11}C	$(10.5 \pm 1.3) \times 10^{-2}$
^{15}O	$(2.1 \pm 0.3) \times 10^{-2}$
259.5 MeV/u	
<i>Nuclei</i>	<i>Experiment</i>
^{10}C	$(1.2 \pm 0.3) \times 10^{-2}$
^{11}C	$(14.7 \pm 1.6) \times 10^{-2}$
^{15}O	$(3.1 \pm 0.4) \times 10^{-2}$
343.46 MeV/u	
<i>Nuclei</i>	<i>Experiment</i>
^{10}C	$(1.5 \pm 0.3) \times 10^{-2}$
^{11}C	$(19.9 \pm 2.4) \times 10^{-2}$
^{15}O	$(5 \pm 0.4) \times 10^{-2}$

Table 4.1: β^+ emitters yields in PMMA

The table 4.1 gives an overview of the experimental production rates of β^+ emitters nuclei induced in a PMMA target and for different incident energies.

4.1.2 Depth profiles

Depth profiles measurement principles are reported in [Priegnitz et al. (2008)]. They are obtained from reconstructed images of a PMMA target irradiation by carbon ions beam for different energies. Only three energies are reported here : 215 MeV/u, 260 MeV/u and 337 MeV/u. The reconstruction algorithm used is filtered back projection including random coincidences correction. Detection efficiency, solid angle and attenuation corrections are also taken into account. These data are shared by the wp6 ENVISION european project.

The experimental depth profiles are illustrated by the figure 4.1. Depth profiles show the spatial distribution of the main β^+ emitter nuclei. Moreover, by integrating the profiles one can determine the total production rates over the whole target.

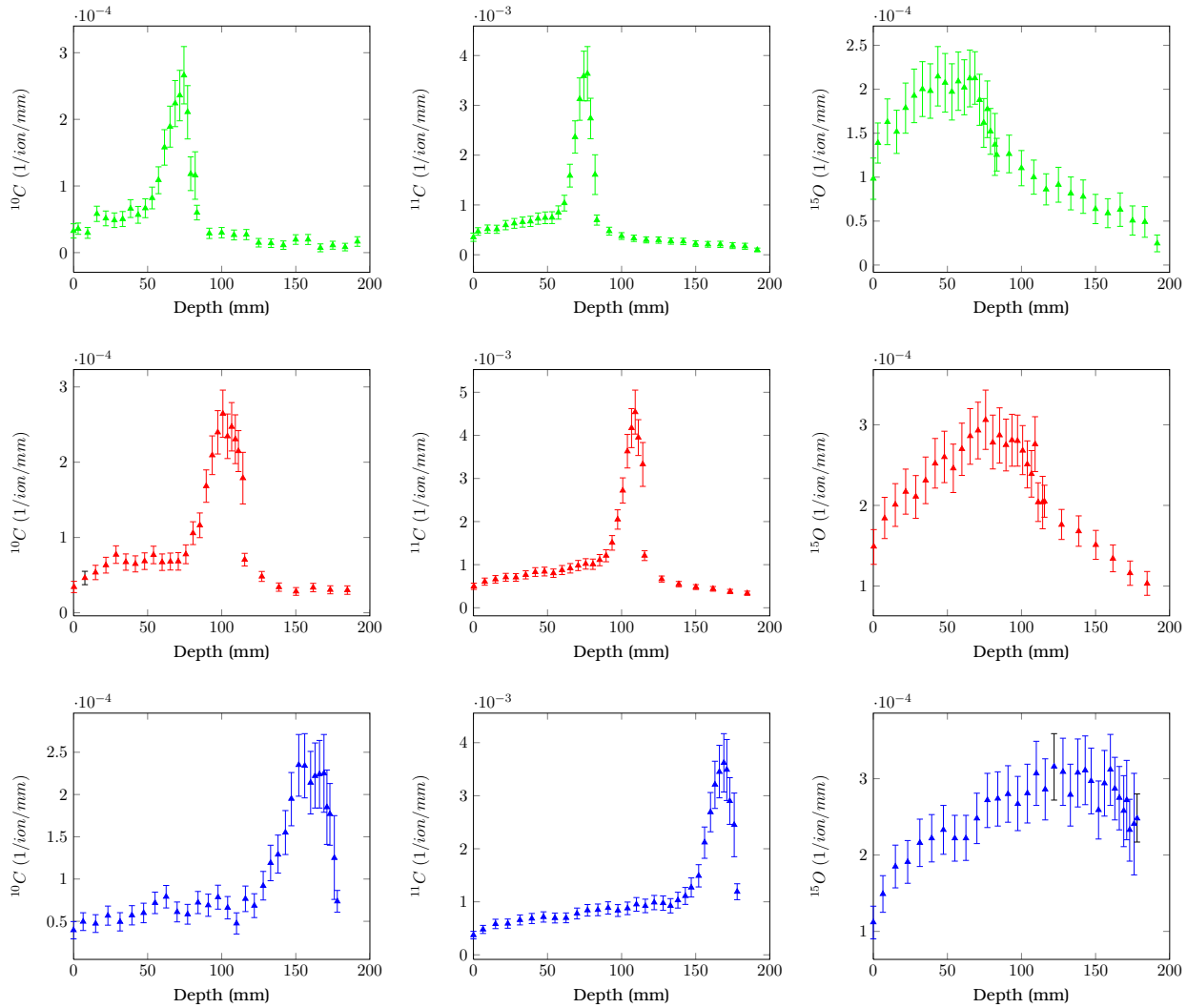


Figure 4.1: β^+ emitter experimental profiles versus depth for 215 MeV/u, 260 MeV/u and 337 MeV/u carbon ions.

Once different experimental data sets have been introduced, we are going to present some comparisons with simulations. They were performed with QMD package since it gives better results for hadrontherapy applications [Böhlen et al. (2010)]. We have divided this comparison study into two steps. The first step is consisting in the simulation of the integrated production rates and their comparison with experimental data. We have considered the measured production rate introduced in the subsection 4.1.1 and the calculated production rates from the depth profiles introduced in the current subsection. The second step will report comparison between simulated and measured production rates versus depth in terms of shape (see section 4.3).

4.2 Total production rates : simulations versus measurements

Total production rates, according to the equation 4.1, were simulated with Geant4. A $90 \times 90 \times 300$ mm³ PMMA phantom was chosen as interacting target. Results are summarized in the table 4.2.

212.12 MeV/u					
	\mathcal{Y}_1	\mathcal{Y}_2	QMD	$\epsilon_{\mathcal{Y}_1}$	$\epsilon_{\mathcal{Y}_2}$
¹⁰ C	$(8 \pm 3) \times 10^{-3}$	$(1.1 \pm 0.3) \times 10^{-2}$	1.0×10^{-2}	25%	9%
¹¹ C	$(10.5 \pm 1.3) \times 10^{-2}$	$(13.9 \pm 0.2) \times 10^{-2}$	9.0×10^{-2}	15%	35%
¹⁵ O	$(2.1 \pm 0.3) \times 10^{-2}$	$(2.8 \pm 0.4) \times 10^{-2}$	2.0×10^{-2}	5%	28%
259.5 MeV/u					
	\mathcal{Y}_1	\mathcal{Y}_2	QMD	$\epsilon_{\mathcal{Y}_1}$	$\epsilon_{\mathcal{Y}_2}$
¹⁰ C	$(1.2 \pm 0.3) \times 10^{-2}$	$(1.7 \pm 0.2) \times 10^{-2}$	1.4×10^{-2}	16%	17%
¹¹ C	$(14.7 \pm 1.6) \times 10^{-2}$	$(24.1 \pm 0.3) \times 10^{-2}$	13.0×10^{-2}	12%	46%
¹⁵ O	$(3.1 \pm 0.4) \times 10^{-2}$	$(5.1 \pm 0.5) \times 10^{-2}$	3.3×10^{-2}	6%	35%
343.46 MeV/u					
	\mathcal{Y}_1	\mathcal{Y}_2	QMD	$\epsilon_{\mathcal{Y}_1}$	$\epsilon_{\mathcal{Y}_2}$
¹⁰ C	$(1.5 \pm 0.3) \times 10^{-2}$	$(2.2 \pm 0.3) \times 10^{-2}$	2.3×10^{-2}	53%	4%
¹¹ C	$(19.9 \pm 2.4) \times 10^{-2}$	$(30 \pm 0.4) \times 10^{-2}$	20.9×10^{-2}	5%	30%
¹⁵ O	$(5 \pm 0.4) \times 10^{-2}$	$(7.8 \pm 0.5) \times 10^{-2}$	5.9×10^{-2}	18%	24%

Table 4.2: β^+ emitter yields in PMMA. \mathcal{Y}_1 refers to production rate given by [I.Pshenichnov et al. (2006)] [Parodi (2005)]. \mathcal{Y}_2 refers to production calculated from depth profiles. Simulations were performed using Geant4 v.9.4.b01 using QMD package. $\epsilon_{\mathcal{Y}_1}$ and $\epsilon_{\mathcal{Y}_2}$ are the relative deviations between QMD and \mathcal{Y}_1 and \mathcal{Y}_2 respectively.

\mathcal{Y}_1 column contains the total production rates given by [I.Pshenichnov et al. (2006)] [Parodi (2005)]. \mathcal{Y}_2 column gives the total production rates calculated from experimental depth profiles. In each case the relative deviations $\epsilon_{\mathcal{Y}_1}$ and $\epsilon_{\mathcal{Y}_2}$ between QMD and each yield were calculated.

As we can see, in each case, results given by simulations are in good agreement with both data sets. We can notice that ^{11}C and ^{15}O simulated yields are in better agreement with \mathcal{Y}_1 whereas ^{10}C simulated yields are in better agreement with \mathcal{Y}_2 . Moreover it seems that \mathcal{Y}_2 are systematically larger than \mathcal{Y}_1 . Further investigations are required to conclude regarding those two experimental data sets.

The total β^+ emitters yields induced by carbone ions in PMMA target for a [200 MeV/u;350 MeV/u] energy range are well reproduced by simulations given both experimental data. Such observable are intergrated production rate over the whole interacting medium. An other important physical observable is the β^+ emitters distribution over the target. In the section bellow comparisons with experimental depth profiles are presented.

4.3 Depth profiles : simulations versus measurements

In the previous section we saw that simulated ^{10}C production rates are in good agreement with \mathcal{Y}_2 whereas ^{11}C and ^{15}O simulated yields are in better agreement with \mathcal{Y}_1 . For this study we are focusing only on the shapes of the profiles. Both experimental data previously introduced were not acquired following the same procedure. \mathcal{Y}_1 experimental yields were obtained from the radioactive decay curves measured after the target irradiation. \mathcal{Y}_2 depth profiles were measured from reconstructed images. But, depth profiles which represent the way the β^+ activity is distributed in the target is much more important than the production rates themselves. Since β^+ activity is deeply correlated to the dose distribution, the activity distribution is crucial.

Since ^{10}C simulated yields are in good agreement with one of the two experimental data sets introduced, whereas ^{11}C and ^{15}O production rates are in better agreement with the other, we have chosen to compare experimental depth profiles to the simulated ones after renormalizing each profile (simulated and experimental) to unity.

After having been renormalized the figures 4.2, 4.3 and 4.4 present comparisons between simulated and measured depth profiles. Simulations were performed with Geant4 using QMD package. Three different incident energies were considered : 215 MeV/u (figure 4.2), 260 MeV/u (figure 4.3) and 337 MeV/u (figure 4.4).

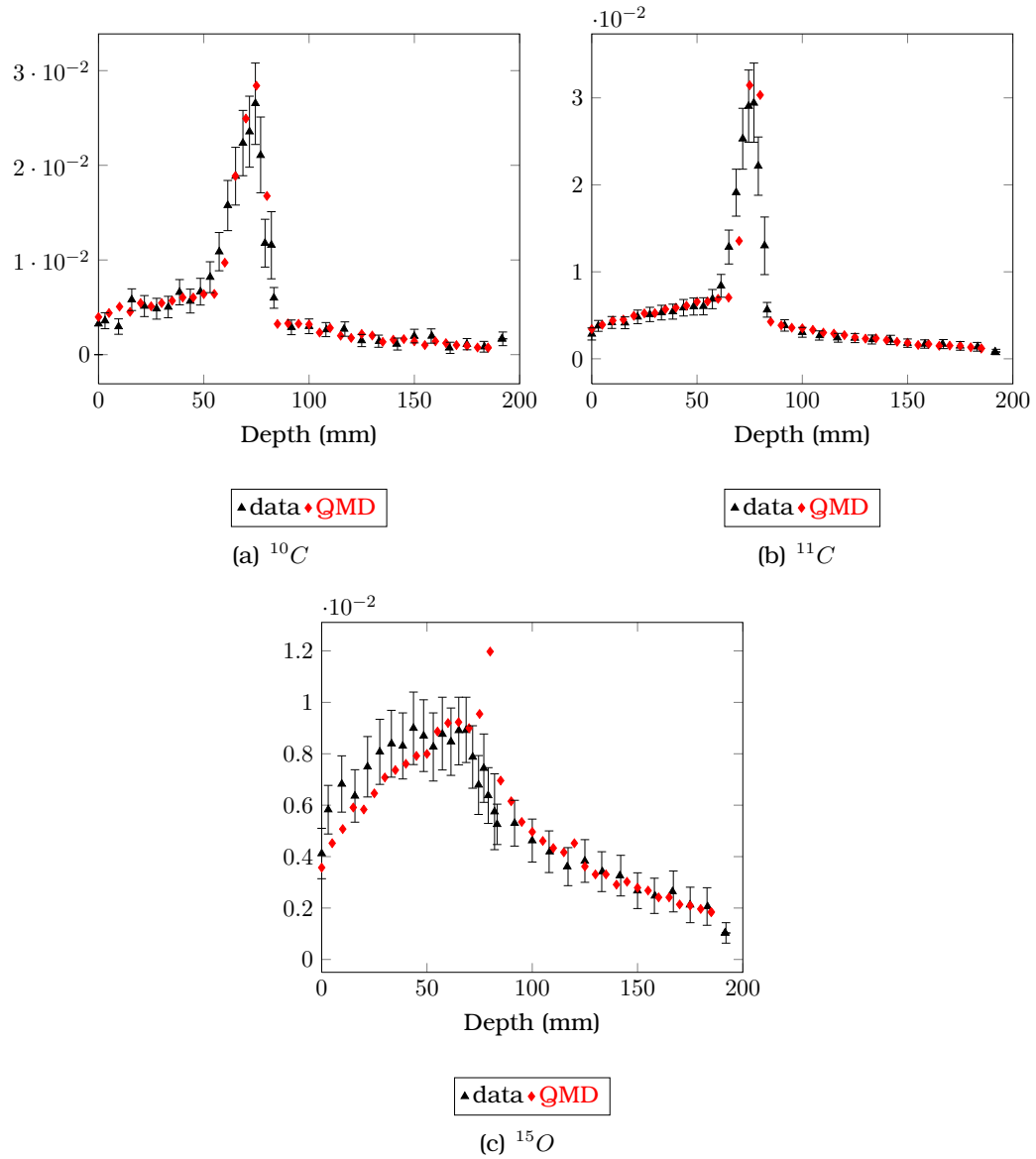


Figure 4.2: β^+ emitter profile versus depth for 215 MeV/u carbon ions. data refers to normalized experimental depth profiles. QMD represents normalized simulated depth profiles using QMD package (v.9.4.b01)

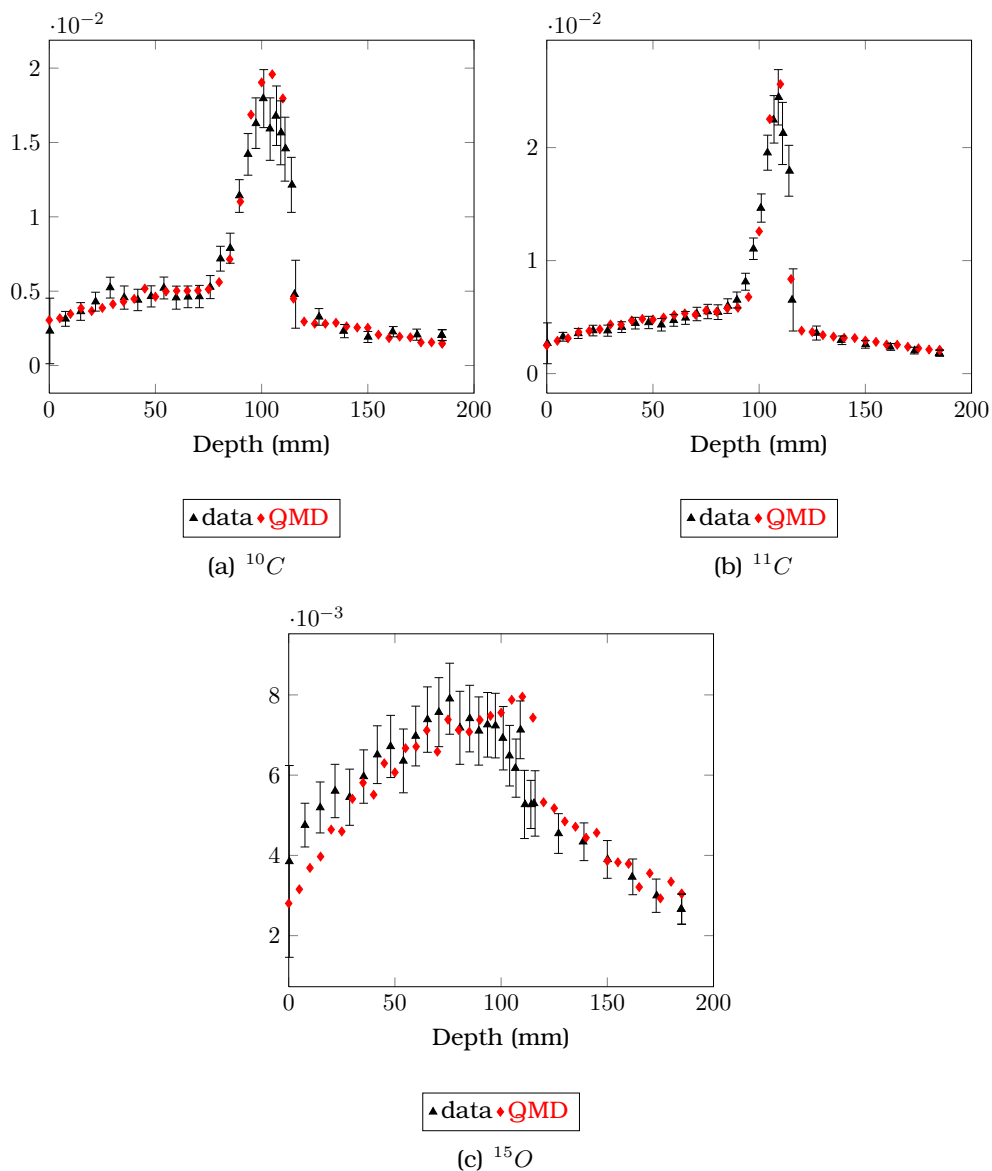


Figure 4.3: β^+ emitter profile versus depth for 260 MeV/u carbon ions. data refers to normalized experimental depth profiles. QMD represents normalized simulated depth profiles using QMD package (v.9.4.b01)

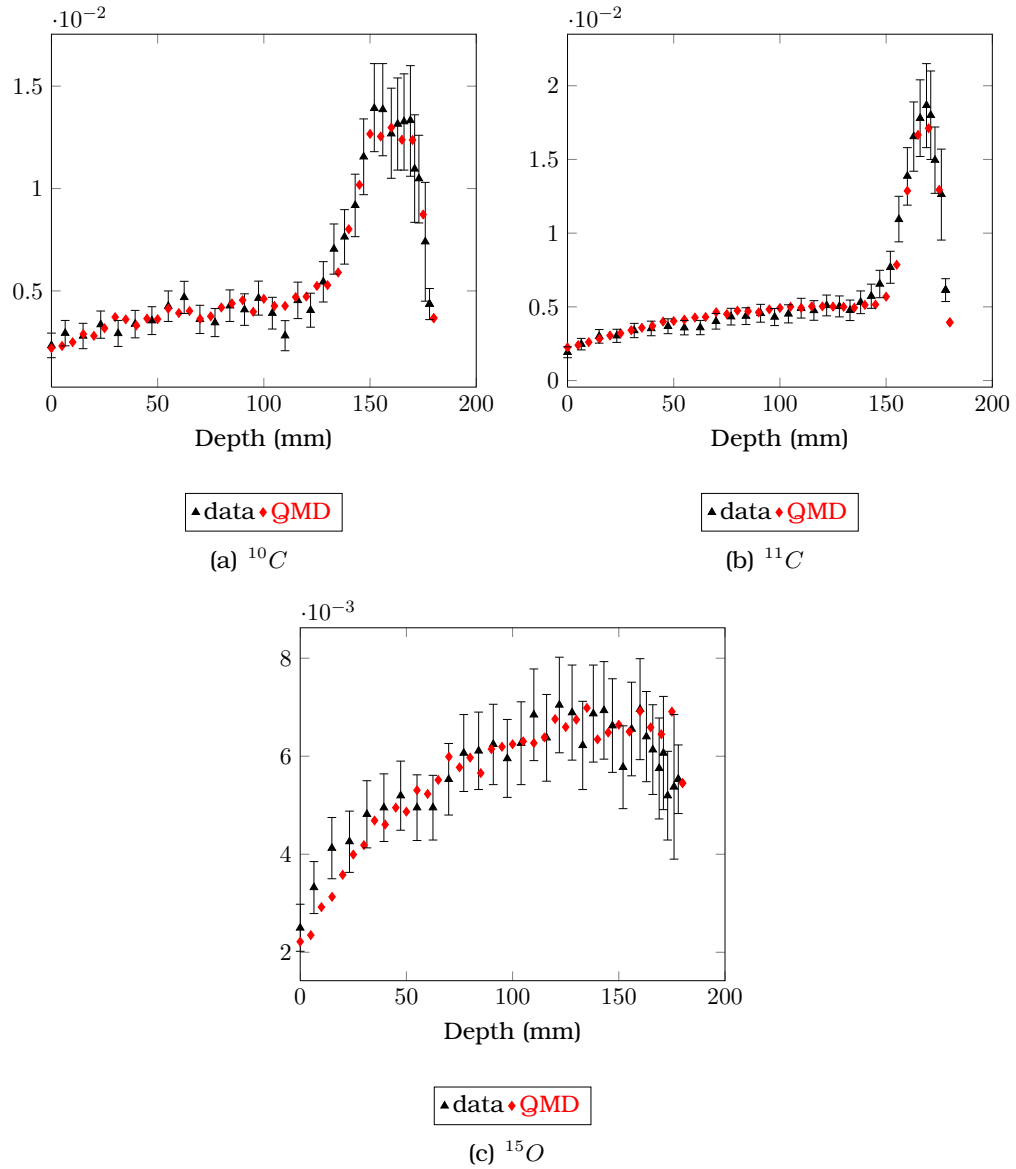


Figure 4.4: β^+ emitter profile versus depth for 337 MeV/u carbon ions. data refers to normalized experimental depth profiles. QMD represents normalized simulated depth profiles using QMD package (v.9.4.b01)

The shapes of the simulated profiles are in quite good agreement with experimental data. One can notice on the ^{15}O simulated profiles there are some little discrepancies near the Bragg pic depth. This point is more obvious from the figures 4.2 and 4.3. Anyway, the shapes are well reproduced which is very promising.

4.4 Discussion

On the one hand β^+ simulated production rates are in good agreement with experimental data. But ^{10}C simulated yields are in good agreement with one of the two experimental data sets introduced, whereas ^{11}C and ^{15}O production rates are in better agreement with the other. Moreover, experimental yields calculated from depth profiles are systematically higher than those measured ($\mathcal{Y}_2 \sim 1.5 \times \mathcal{Y}_1$).

On the other hand simulated depth profiles are in rather good agreement with experimental measurements in terms of shape. Depth profiles shape was the only criterion used to perform comparisons because we probably missed something concerning the understanding of the experimental depth profiles.

In conclusion, Geant4 QMD package gives encouraging results in terms of β^+ emitters nuclei production rates. The shapes are rather well reproduced. Concerning the total production rates, further investigations are however required. If we only consider the experimental depth profiles (see section 4.1.2, ^{11}C and ^{15}O simulated profiles have to be weighted by a factor of 1.5 approximately ($\mathcal{Y}_2/\mathcal{Y}_1$, cf. table 4.2). In case we consider production yields (see section 4.1.1), ^{10}C simulated profiles have to be weighted by a factor of 0.6 approximately ($\mathcal{Y}_1/\mathcal{Y}_2$, cf. table 4.2). If we focus on both experimental data it is impossible to conclude.

Chapter 5

Prompt γ yield

During irradiation, a part of all γ resulting from positron annihilation are produced simultaneously with a lot of secondary particles. Among them prompt γ can be considered as physical background event regarding the PET principle detection. In order, to design a dedicated device able to control the treatment, it is very important to have an accurate estimation of secondary prompt γ yield.

5.1 Prompt γ depth profile : present status

Prompt γ imaging for the dose profile monitoring has been already investigated by Testa et al. [Testa et al. (2008)], [Testa et al. (2009)]. First experiments performed at Ganil in Caen (France) paved the way of real time monitoring carbon therapy treatments. Prompt γ depth profiles simulations have already been performed by Le Foulher et al [Foulher et al. (2010)]. Two different experiments were done by the same group. The first experiment was held at Ganil facility in Caen to measure the prompt γ depth profile induced by a 95 MeV/u carbon ions beam in a PMMA target. The second experiment was held at GSI facility in Darmstadt (Germany) to measure the the prompt γ depth profile induced by a 310 MeV/u carbon ions beam in a water target.

Each experimental set-up was designed to detect prompt γ emitted at 90 degrees of the beam direction. Only prompt gammas that deposited more than 1 or 2 MeV in the detector, in a few ns Time of Flight (TOF) window were recorded [Foulher et al. (2010)]. Since a lot of secondary neutrons are induced by nuclear collisions, this TOF technique was introduced to discriminate these neutrons from the prompt γ . Both experimental set-up are shown in figure 5.1.

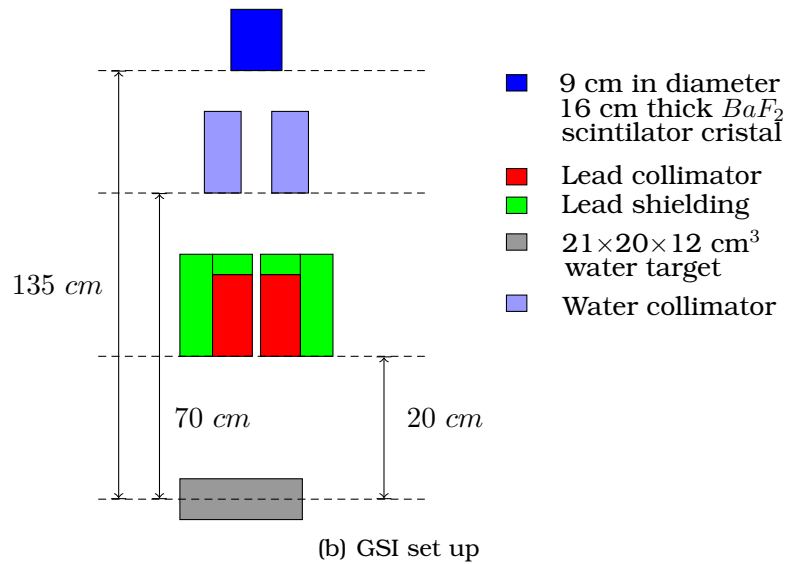
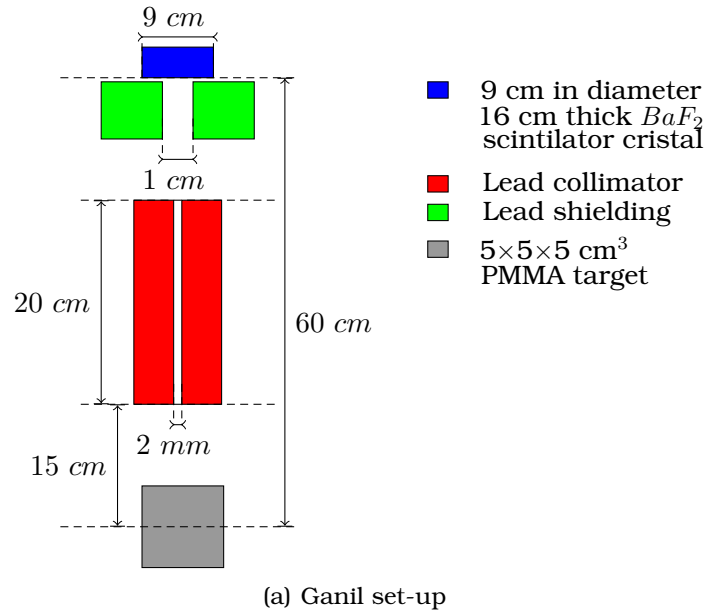


Figure 5.1: Experimental set-up dedicated to the prompt γ depth profiles measurement. (a) Ganil set-up : 95 MeV/u carbon ions on PMMA target. (b) GSI set-up : 310 MeV/u carbon ions on water target. [Foulher et al. (2010)]

The physics list used was composed of binary cascade model to handle nuclear collisions, precompound model used as a smooth transition, Evaporation model to deexcite fragments and Photon emission model to finish the deexcitation chain. Geant4 v.9.1. was used to perform simulations and reproduce the experimental data. The results of the simulations performed by Le Foulher *et al.* are shown on the figure 5.2.

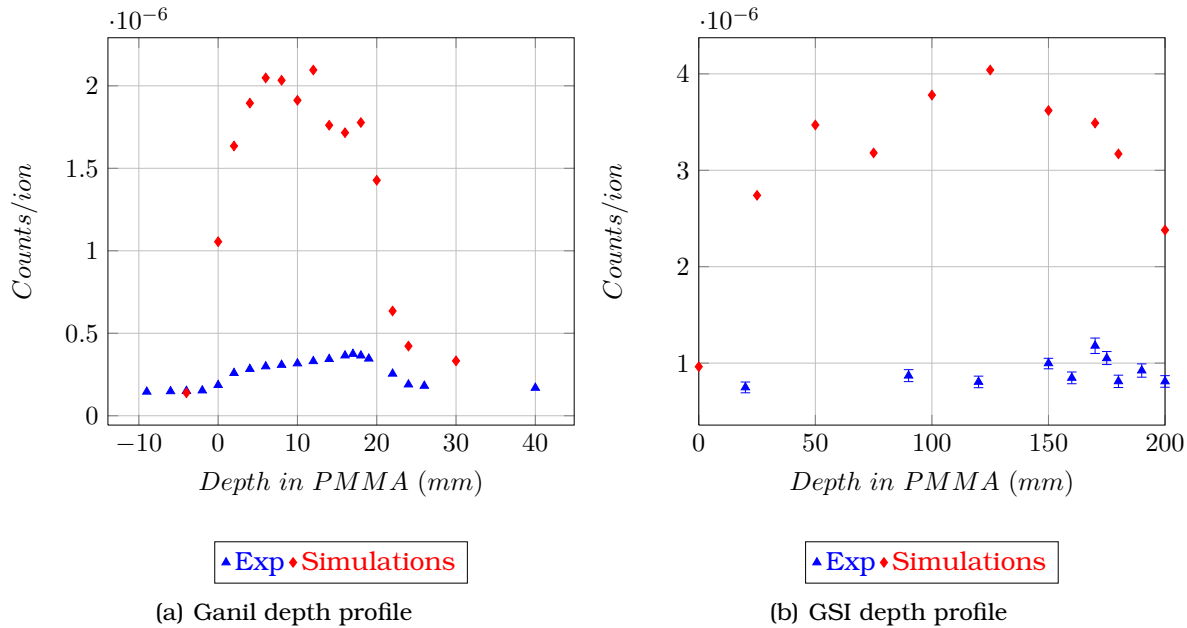


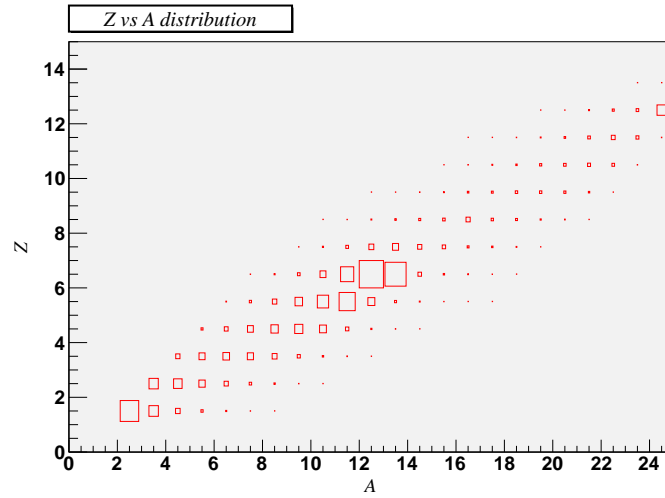
Figure 5.2: Measured versus simulated prompt γ depth profile. (a) Ganil experiment. (b) GSI experiment. In each case *Exp* refers to the measurements [Foulher *et al.* (2010)].

As illustrate in the figure 5.2 simulations overestimates largely the experimental prompt γ rate. Moreover, the shapes of the profiles are not well reproduced. In order to understand the nature of those discrepancies, we have to focus on the deexcitation methods since they handle the prompt γ emission. For our study one used the version 9.2 of the Geant4 toolkit.

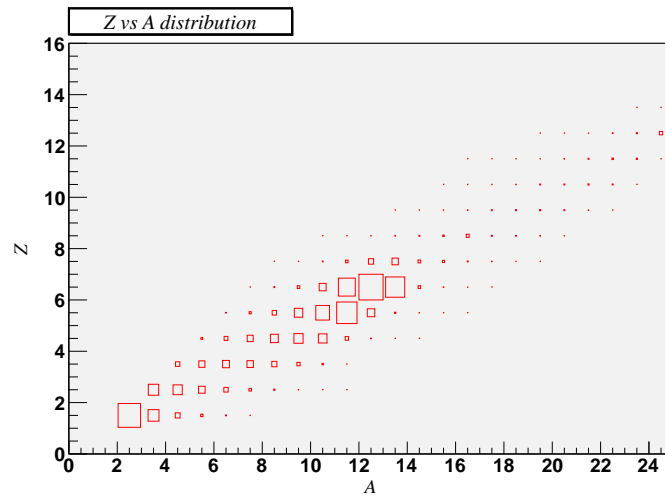
5.2 Excited fragments spectrum

We have performed preliminary studies that consisted in characterize the excited fragments spectrum in terms of mass A , charge Z and excitation energy E^* produced during $^{12}C - ^{12}C$ for 75 MeV/u and 200 MeV/u incident energies. Processes which are supposed

to be involved in the deexcitation procedures have been thus clearly identified. The figures 5.3 and 5.4 present Z versus A and A versus E^* spectra obtained using the Geant4 v.9.2 QMD package.

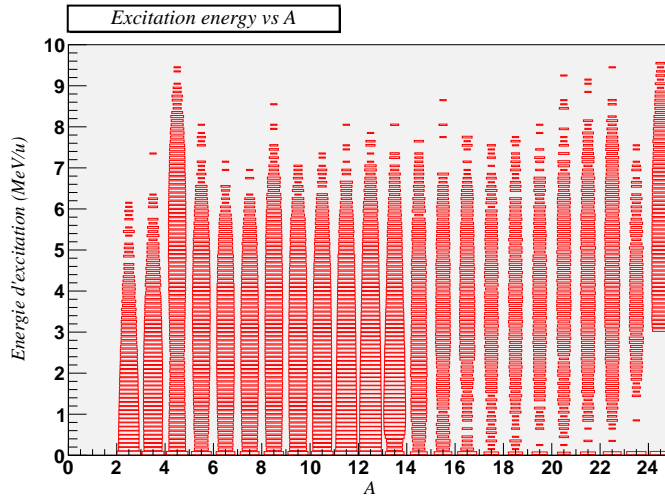


(a) 75 MeV/u

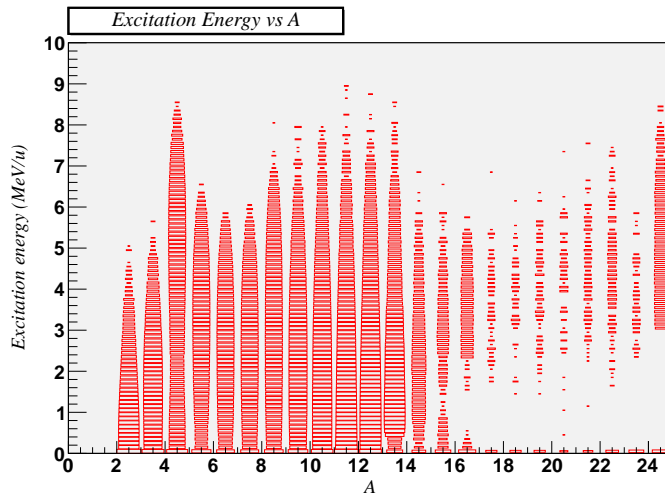


(b) 200 MeV/u

Figure 5.3: Z versus A spectrum of the QMD Geant4 v.9.2 simulated fragments population produced during $^{12}\text{C} - ^{12}\text{C}$ collisions at 75 MeV/u (a) and 200 MeV/u (b)



(a) 75 MeV/u



(b) 200 MeV/u

Figure 5.4: E^* versus A spectrum of the QMD Geant4 v.9.2 simulated fragments population produced during $^{12}\text{C} - ^{12}\text{C}$ collisions at 75 MeV/u (a) and 200 MeV/u (b)

As shown in the figures 5.3 and 5.4, the excited fragments population is mainly composed of light fragments with $Z \leq 7$ and $A \leq 14$. Those fragments have to be deexcited by Fermi BreakUp process. The heavier fragments have to be treated according to Evaporation process.

5.3 Deexcitation chain

The **G4ExcitationHandler** class handles all the deexcitation models. The default class of the Geant4 toolkit has been described in the section 3. Here some results obtained with this default class are presented.

5.3.1 G4ExcitationHandler default class

We consider the prompt γ energy spectrum and the prompt γ emission rate during deexcitation. Photon emission is treated exclusively during deexcitation. One can distinguish 5 different modes of γ depending on the way they are produced.

The two first production modes consist of photons emitted through evaporation process. There are discrete emitted photons which are coming from quantized transitions and also continuous emitted photons from dipole transition consequently to giant dipole resonances.

The two second production modes are compound of discrete and continuous emitted photons too. But, unlike the two first types, those photons are produced at the end of the deexcitation chain, after Fermi BreakUp or Evaporation processes.

The last production mode of photons is the “forced” γ . An artificial final photon emission is performed if photon evaporation can’t deexcite fragments. The table 5.1 sums up the contribution of each type of photons in the total spectrum.

75 MeV/u				
<i>Continuous Evaporation</i>	<i>Discret Evaporation</i>	<i>Continuous PhotonEvaporation</i>	<i>Discret PhotonEvaporation</i>	<i>Forced Emission</i>
4.10^{-4}	2.10^{-3}	7.10^{-2}	8.10^{-2}	12.10^{-2}
200 MeV/u				
<i>Continuous Evaporation</i>	<i>Discret Evaporation</i>	<i>Continuous PhotonEvaporation</i>	<i>Discret PhotonEvaporation</i>	<i>Forced Emission</i>
3.10^{-4}	1.10^{-3}	9.10^{-2}	33.10^{-2}	80.10^{-2}

Table 5.1: Prompt γ spectrum description . Geant4 v.9.2 simulated $^{12}\text{C} - ^{12}\text{C}$ collisions

The main component is the forced γ component. This point is confirmed by the figures 5.5 and 5.6. This can be explained as followed.

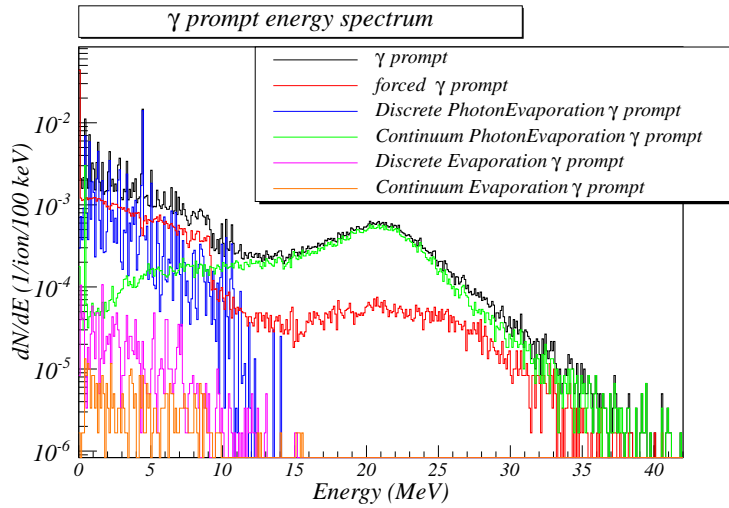


Figure 5.5: Simulation of prompt γ energy spectrum in $^{12}\text{C} - ^{12}\text{C}$ collisions at 75 MeV/u

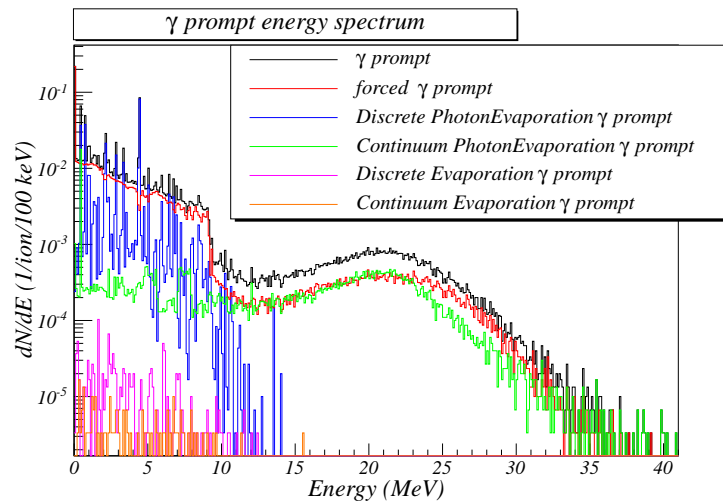


Figure 5.6: Simulation of prompt γ energy spectrum in $^{12}\text{C} - ^{12}\text{C}$ collisions at 200 MeV/u

On the one hand, light clusters ($A \leq 4$) are not deexcited by Fermi BreakUp. They are

only deexcited by *PhotonEvaporation*. But any nuclear transition is impossible since the database does not exist for such light nuclei. Indeed, nuclear transitions are tabulated from the *PhotonEvaporation2.0* database. So, every light excited clusters are deexcited by “forced” emission. Moreover, their contribution is not negligible as shown in figures 5.3, 5.4.

On the other hand, excitation energy of fragments produced by *Fermi BreakUp* is supposed to be quantized. The *Geant4* method which manages this quantization is the ***G4FermiBreakUp:: G4FermiFragmentPool***. A look at this class shows that energy units are keV not MeV. Moreover, there is a mismatch between values from the *PhotonEvaporation2.0* database and those which are given by the ***G4FermiFragmentPool*** method. This have some consequences because, some fragments after *Fermi BreakUp* can be only deexcited by “forced” emission since nuclear level do not coincide with the one listed in the *Geant4* database.

Those two points show that are some modifications have to be done in order to reduce the simulated prompt γ emission rate, just because some γ are coming from unphysical processes. In the next section we are going to present in detail modifications introduced in the code and the consequences on the γ emission rate.

5.3.2 New handler algorithm

The new algorithm is divided into two different steps. One step handles the deexcitation through *Fermi BreakUp* and/or *Evaporation* as shown in figure 5.7.

At the end of this first step, one can distinguish two different types of fragments : unexcited fragments which are stored as the final products of the reaction and excited fragments which are going to be deexcite through *PhotonEvaporation* process. The algorithm which is used to handle the different step *PhotonEvaporation* process is illustrated on the figure 5.8.

The table 5.2, and the figures 5.9 and 5.10 show energy spectrum obtained with this new handler and the contribution of each photon depending on their production mode. One can note some important changes.

The first change is that there is no more “forced” γ . The second change we can observe is that photons coming from nuclear transitions are the main photons of the total spectrum since *Fermi BreakUp* is the main deexciting process.

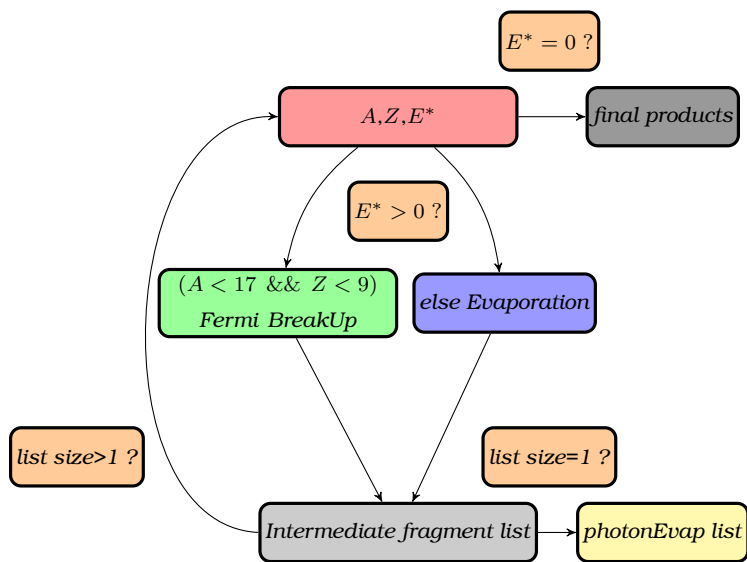


Figure 5.7: First step of the deexcitation. Only Fermi BreakUp and Evaporation are considered.

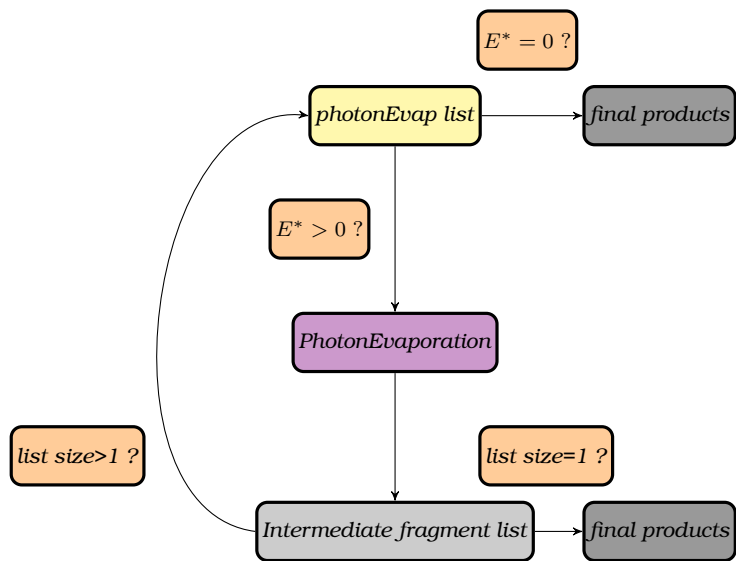


Figure 5.8: Second step of the deexcitation chain. Only PhotonEvaporation is considered.

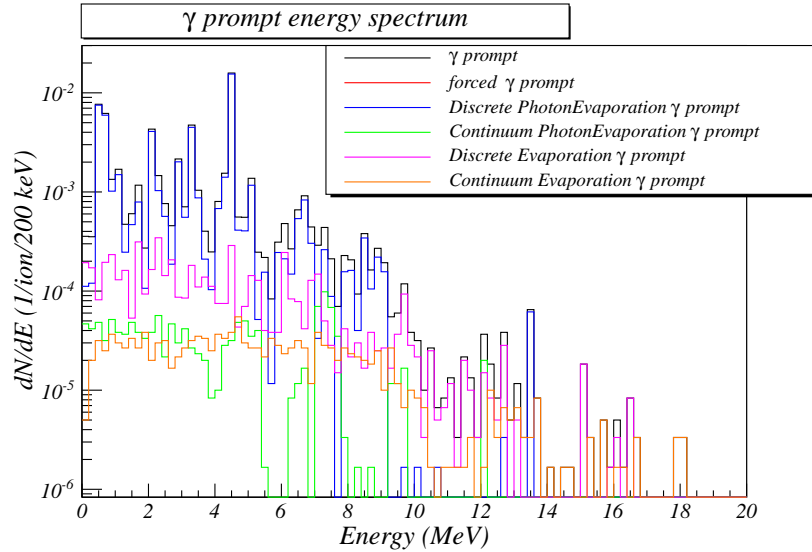


Figure 5.9: *Geant4 v.9.2 simulated prompt γ energy spectrum for $^{12}\text{C} - ^{12}\text{C}$ collisions at 200 MeV/u. The new handler algorithm is used to handle the deexcitation chain*

The energy range of the emitted γ is quite reduced too. Since *Fermi BreakUp* process is preferred given the mass spectrum of the primary fragments, nuclear transitions reaction is the natural process which follows. But, despite the discrete photon relative contribution coming from *PhotonEvaporation* is larger with this new algorithm, the number (normalized by the primary ion number) of this type of photon is not larger. By way of contrast the continuous *PhotonEvaporation* photons yields are significantly reduced.

We can give an explanation from the figure 5.11. This figure shows the excitation energy versus mass distribution of fragments just before the *PhotonEvaporation* process for two different incident energies (75 MeV/u and 200 MeV/u) and for the two different handler.

The default handler gives heavy high excited fragments which will be deexcited through continuous *PhotonEvaporation*. The new handler algorithm lead to the deexcitation of those heavy excited fragments. That's why continuous *PhotonEvaporation* γ yield is much more important in case of default handler.

75 MeV/u				
Continuous Evaporation	Discret Evaporation	Continuous PhotonEvaporation	Discret PhotonEvaporation	Forced Emission
1.10^{-3}	5.10^{-3}	1.10^{-3}	5.10^{-2}	0
200 MeV/u				
Continuous Evaporation	Discret Evaporation	Continuous PhotonEvaporation	Discret PhotonEvaporation	Forced Emission
1.10^{-3}	4.10^{-3}	1.10^{-2}	33.10^{-2}	0

Table 5.2: Total spectrum obtained with the new handler

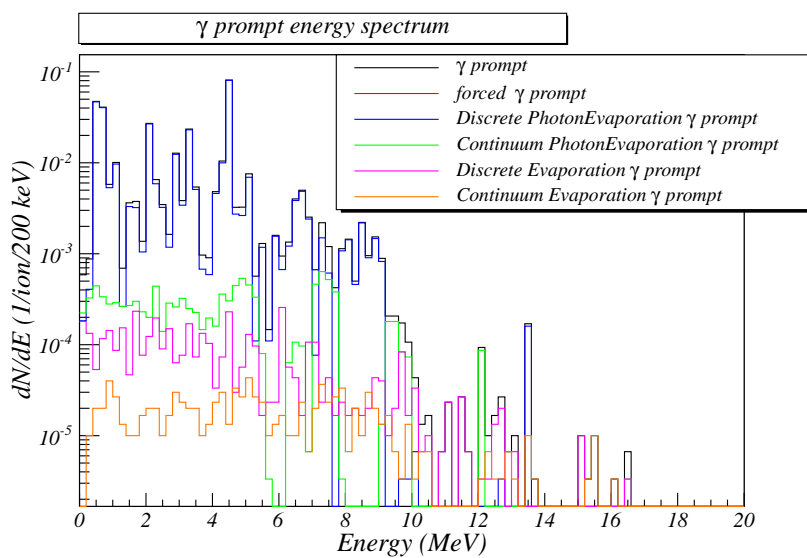


Figure 5.10: Geant4 v.9.2 simulated prompt γ energy spectrum for $^{12}\text{C} - ^{12}\text{C}$ collisions at 200 MeV/u. The new handler algorithm is used to handle the deexcitation chain

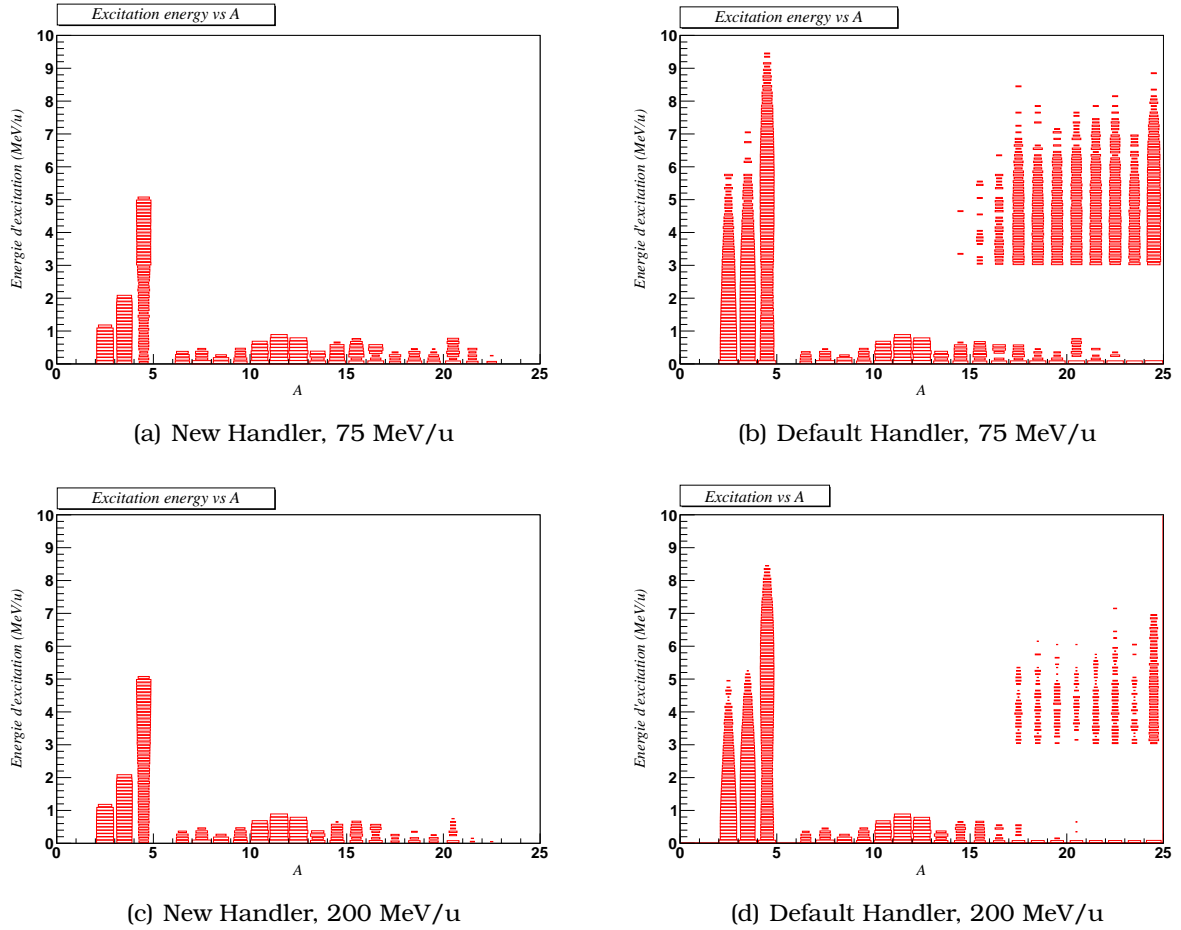


Figure 5.11: Excitation energy versus A diagram for QMD Geant4 v.9.2 simulated fragments population produced during $^{12}\text{C} - ^{12}\text{C}$ collisions at 75 MeV/u (a) (b) and 200 MeV/u (c) (d). Results are obtained using the two different handler

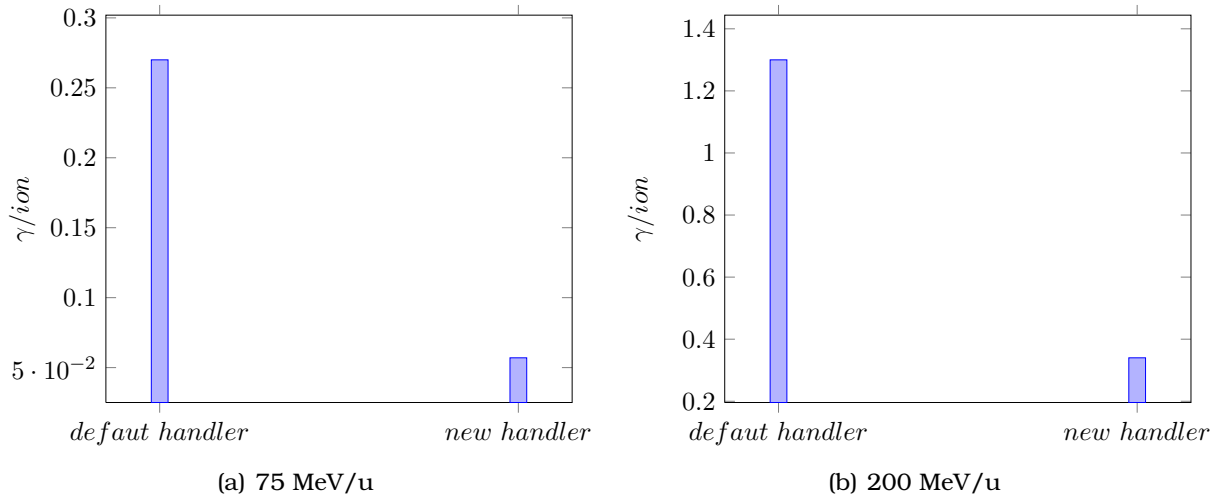


Figure 5.12: Total Geant4 v.9.2 simulated γ yields ((a) 75 MeV/u, (b) 200 MeV/u) with the two different handler

The figure 5.12 shows the total prompt γ yield for two incident energies obtained with the two handler. The new handler reduces by a factor 5 the total simulated prompt γ yield.

The figure 5.13 presents the secondary particle yields ($p, n, d, t, {}^3He, {}^4He, {}^{10}C, {}^{11}C$) produced by ${}^{12}C - {}^{12}C$ collisions simulated with Geant4 v.9.2. This new handler produces a little bit more light clusters such as p, n, d and 4He . In fact, Fermi BreakUp model is the main deexcitation process and it is a more or less explosive like process. This leads to split fragments via the emission of light clusters. However, yields are not very different which means this new algorithm impacts significantly on photon yield only.

To complete this study one can consider the excitation state of fragments at the end of the deexcitation chain. The figure 5.14 shows the excitation state of the final simulated fragments ((a) for 75 MeV/u incident energy and (b) for 200 MeV/u incident energy). Some fragments are not completely deexcited. Those fragments account for $\sim 15\%$ of the total secondary particles produced by nuclear collisions. QMD and statistical deexcitation models do not take into account nuclear spin orbit neither pairing couplings between nucleons.

However such kind of interaction are very important since they govern the nuclear

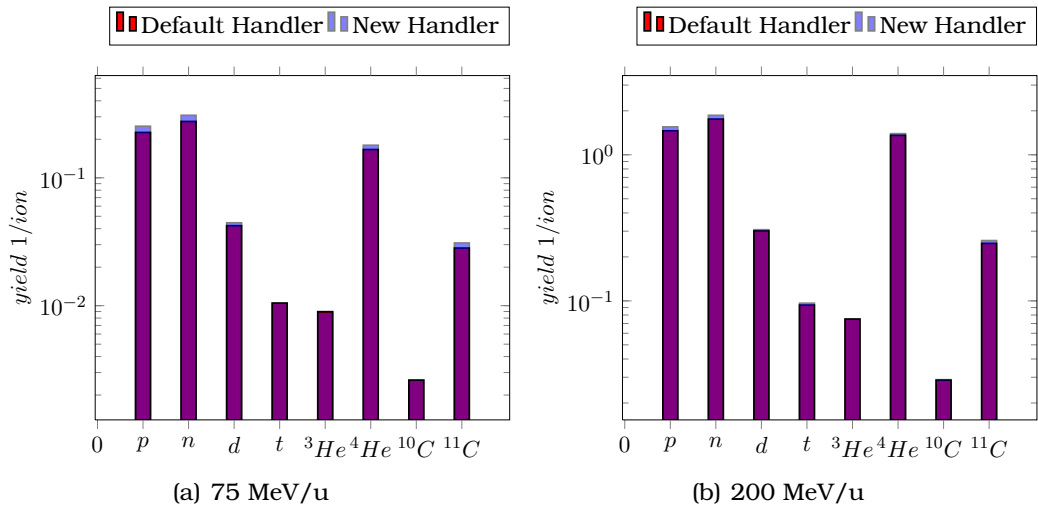


Figure 5.13: Secondary particle Geant4 v.9.2 simulated yield for $^{12}\text{C} - ^{12}\text{C}$ collisions at 75 MeV/u (a) and at 200 MeV/u (b) with the two different handler

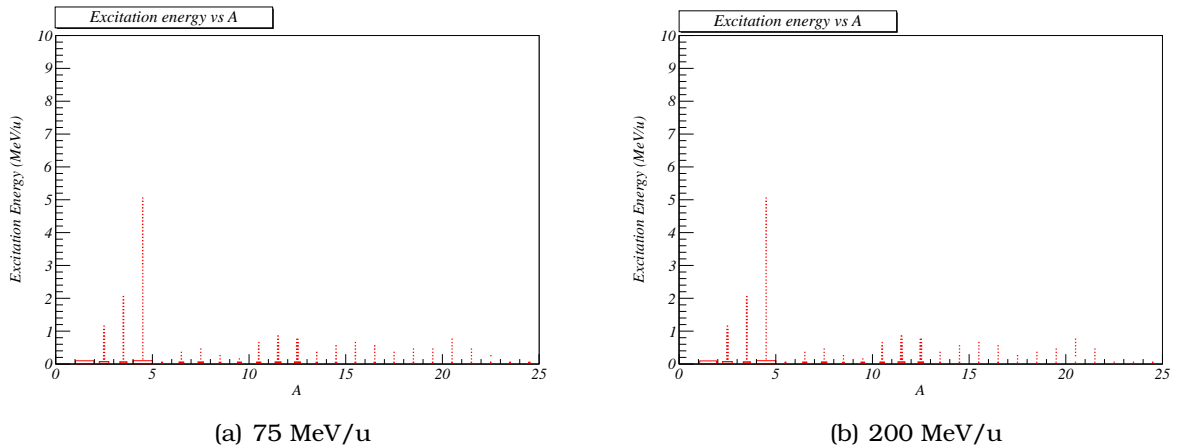


Figure 5.14: Geant4 v.9.2 simulated excitation energy versus A diagram at the end of the whole deexcitation for excited fragments population produced during $^{12}\text{C} - ^{12}\text{C}$ collisions at 75 MeV/u (a) and at 200 MeV/u (b)

structure. For instance the experimental pairing gaps are reproduced by the formula :

$$\Delta \approx 12A^{-1/2} \text{ MeV} \quad (5.1)$$

For light clusters, pairing gaps account for few MeV which is comparable to the residual excitation energy. On the other hand, ground state calculated are not the true ground state since they are calculated in order to fit nuclear saturation point ($\rho = \rho_0$ and $E = -15.75 \text{ MeV}$). In conclusion given all these arguments this is not a real problem to have some fragments with a small residual excitation energy.

Until now were presented some modifications introduced to reduce prompt γ production. Comparisons with experimental data are required to validate those modifications. In the following section, simulations were performed with the last released Geant4 version (9.4). This report were initiated before this version was available. Some modifications were introduced (compared to the previous versions) in the **G4ExcitationHandler** class and **G4PhotonEvaporation** classes. However, the new **G4ExcitationHandler::BreakItUp0** method still remain different from our own modified method. In fact, despite Fermi BreakUp model is extended to the light excited clusters such as ${}^4\text{He}$ or t , the Evaporation model is called in case Fermi BreakUp can not deexcite fragments. In those precise cases, we have noticed that the photon evaporation channel is always chosen. Moreover, the method used to perform the photon evaporation process produces only one photon. As a consequence, there is no photon emitted when fragments are processed by the last photon emission loop. That's why we choose to implement our own **G4ExcitationHandler::BreakItUp()** method in the last released Geant4 version.

5.4 Simulations vs measurements

5.4.1 Preliminaries

Before discussing comparison between simulations and Ganil experimental results explain the nuclear level selection procedure as implemented in the **G4PhotonEvaporation** classes. This selection procedure is performed by the **NearestLevel** method from the GEANT4 class **G4NuclearLevel**. This method takes two arguments. The first one is the excitation energy of the fragment whereas the second argument is an artificial tolerance.

Basically, a radiative transition is allowed when the difference between the excitation energy and a level found in the nuclear database is below the tolerance.

It is possible to tune this artificial tolerance. In case there is a large tolerance, the closer tabulated level is chosen even if the difference between the excitation energy and the tabulated one is huge, e.g. 2 MeV. On the other hand, if the tolerance is very low,

only fragments which the excitation is strictly quantized will be deexcited. By default, this tolerance is very large (10 TeV), which means there is no constraint on the transition selection.

5.4.2 Ganil experiment

The figure 5.15 shows comparison between simulations and the Ganil experiment results.

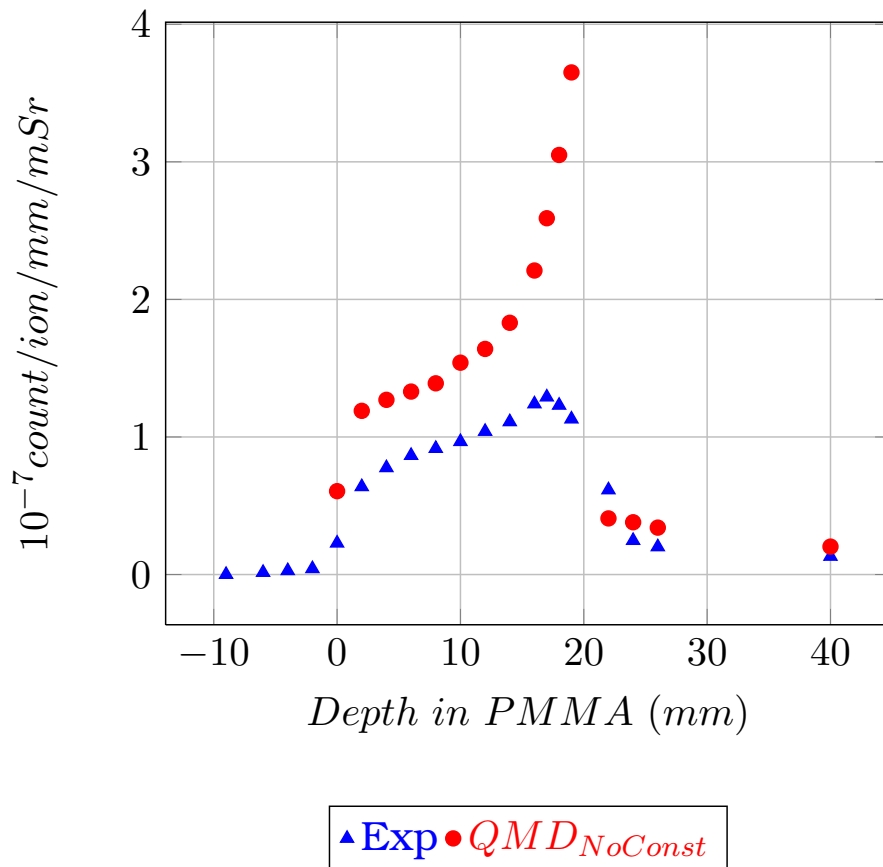


Figure 5.15: Measured versus Geant4 v.9.4.b01 + new handler simulated prompt γ depth profile: $95 \text{ MeV/u } {}_{6}^{12}\text{C}^{6+}$ on PMMA target at the GANIL

The blue plot refers to the measured prompt γ yield as a function of depth in the PMMA target whereas the red plot refers to the simulated depth profile using QMD package. The

tolerance value chosen is the default one. As we can see, simulation overestimates by a constant factor of 1.5 upstream the Bragg peak depth and by a factor of 3 at the Bragg peak depth.

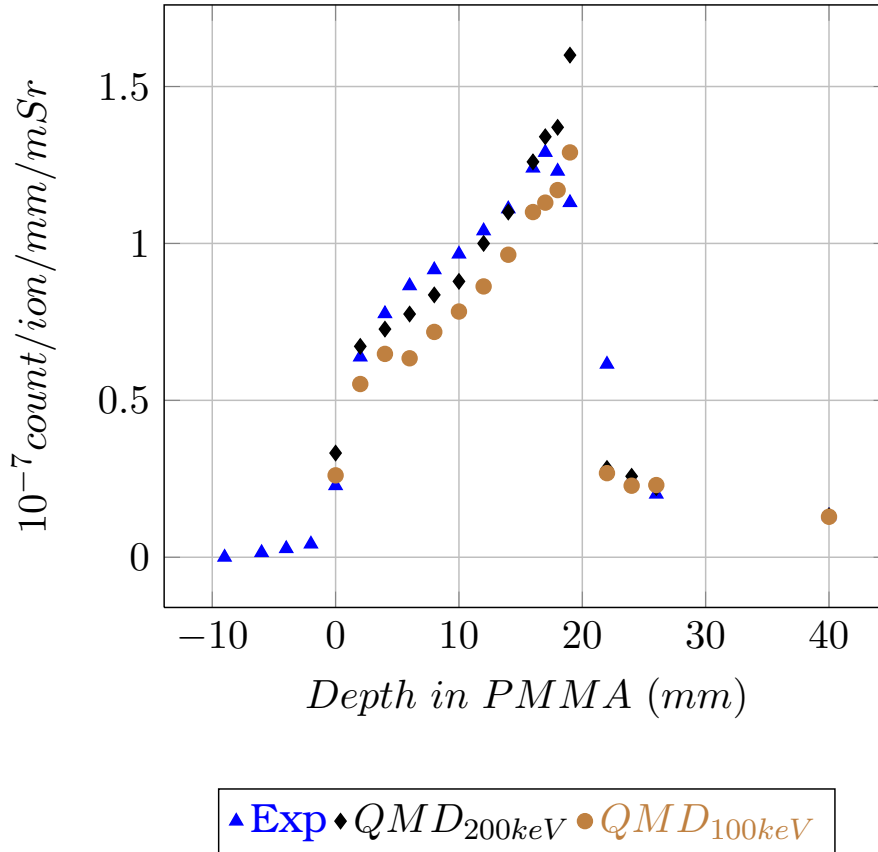


Figure 5.16: Measured versus Geant4 v.9.4.b01 + new handler simulated prompt γ depth profile: $95 \text{ MeV/u } {}_{6}^{12}\text{C}^{6+}$ on PMMA target at the GANIL

The figure 5.16 shows comparisons between measured and simulated data for several tolerance value : 100 keV (brown plot) and 200 keV (black plot).

Simulations are in rather good agreement with experimental data for a 200 keV tolerance value. Shape is well reproduced despite a small discrepancy near the Bragg peak depth. But this deviation is no larger than few dozen percent which is in much more better agreement than previous results.

By tuning the nuclear level selection procedure, we are able to to reproduce Ganil

experimental data. The prompt γ rays at 95 MeV/u are well reproduced. However, we do not know if this energy level selection procedure tolerance value will give good agreements at higher energies and for different targets and projectiles.

5.4.3 GSI experiment

Consider experimental results obtained at GSI in Darmstadt for carbon ions at 310 MeV/u interacting with a water phantom. The figure 5.17 shows measured and simulated depth profile. Simulations were performed with the QMD package, and the modified handler. Two tolerance values were considered : a 200 keV tolerance (red plot) and the default one (black plot).

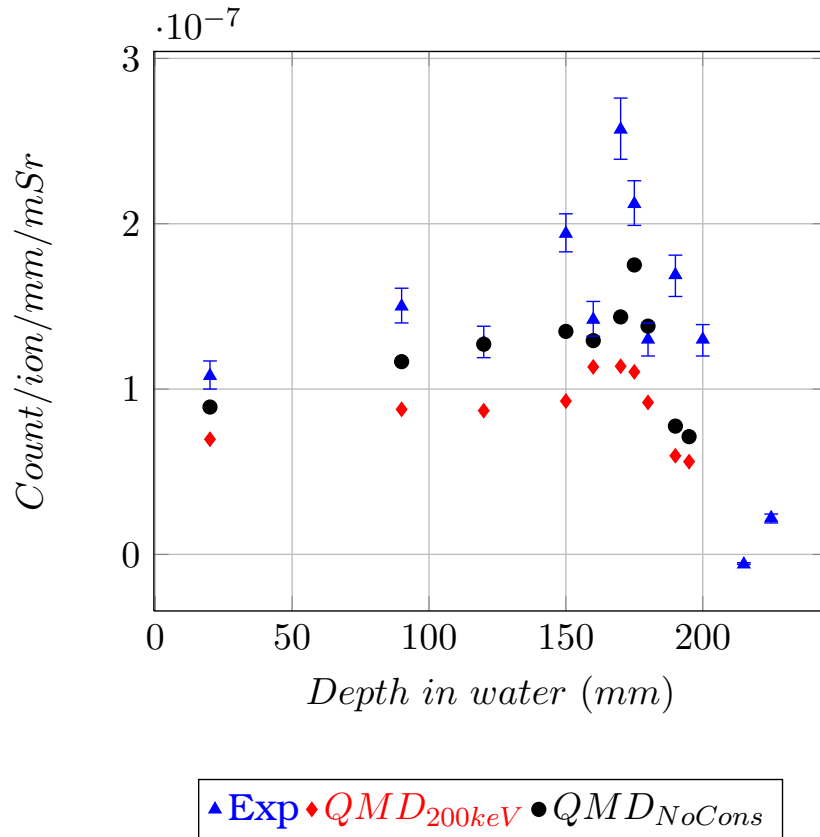


Figure 5.17: Measured versus simulated prompt γ depth profile : 310 MeV/u $^{12}\text{C}^{6+}$ on water target at the GSI

At this energy range, we can observe that the prompt γ detection yield is less sensitive to the level tolerance value than at low energy (~ 100 MeV/u, cf. previous section). Simulations with a 200 keV tolerance and with a 10 TeV tolerance are very close. This point is very interesting. Since results are very similar whatever the tolerance, is it reasonable to choose a 200 keV tolerance value whatever the incident energy of the primary ions. In conclusion, the new handler gives quite good results. The prompt γ yield is significantly reduced. However, we have to mitigate one point. We have introduced a parameter in order to control the prompt γ production rate. This is quite dubious since this tolerance create band gaps. In fact, any fragment with an excitation energy out of this energy band will not be deexcited.

On the other hand, this tolerance is a way to control the photon emission. If any constraint is added to the selection procedure, any fragment with a little excitation energy will be deexcited. This leads to produce too much prompt γ . This tolerance is a kind of trick but not a real physical solution. The correct solution should be to modify the nuclear collision models to avoid the formation of such fragments. This observation requires further measurements and simulations.

Conclusion

The section 1 has presented different type of nuclear collision models. More precisely, QMD model was developed and each ingredient of the model were introduced. QMD was preferred to other nuclear models since it gives for now the best results for hadron-therapy applications. Moreover, it is a theoretically able to simulate low energy nuclear collisions because it takes mutual interactions through Skyrme potential into account.

The section 2 was dealing with the different models used to describe the fragment de-excitation. Fermi Break model is suitable to deexcite light fragments ($A < 16$). Evaporation model seems more appropriate to the treatment of heavier fragments. The different channels can be divided into three components : particles evaporation (p, n, d, t, ${}^3\text{He}$, ${}^4\text{He}$ and heavier cluster such as ${}^{29}\text{Mg}$), photon evaporation essentially governed by the giant dipole resonances, and the competitive fission. In order to complete the deexcitation, an additional photon emission based on nuclear radiative transition is also suitable. Fermi BreakUp and nuclear transition seem dedicated to the deexcitation of fragments induced by nuclear collisions between biological element (O,C,H,N).

The section 3 was dedicated to the description of the implementation of the previously presented models in the Geant4 monte carlo toolkit.

The section 4 has reported β^+ emitter production yield simulation and comparison with experimental data. QMD package was used for the simulations. Simulations provide good results in comparisons with experimental data. However, we can not compare simulations with data acquired at low energy (< 100 MeV/u) because of the lack of measurements. This point will be investigated later since an experiment is planned in the current year to provide such data for 95 MeV/u carbon ions beam at Ganil in Caen.

The section 5 we have investigated the present status on prompt γ ray. We have investigated on the the prompt γ yield reduction and provide some comparisons with measured data. Simulations give good result at 95 MeV/u and and at 310 MeV/u but further measurements especially at 310 MeV/u are required to conclude properly.

Results presented in the sections 4 and 5 are relatively consistent regarding the experimental data. Annihilation γ and prompt γ are well reproduced in terms of spatial distribution and production yields. The proper estimation of those two types of particles are very important for the conception of a PET based device to the control of hadrontherapy treatment.

This document was initiated in order to summarize all the work we have done on Monte Carlo simulations dedicated to hadrontherapy applications. We are concerned by R&D on TOF PET detectors. The proper estimation of secondary particles produced counting rates is crucial. Only QMD model was investigated. Despite the other nuclear collision models available in Geant4, such as binary cascade model, QMD model is the more precise for particle therapy energy range. However, it is clear that those models were not conceived to study carbon ion fragmentation at about a hundred MeV/u.

Many groups in Europe are working on Monte Carlo simulations for particle therapy purposes and they need accurate simulation tools. Geant4 gives good results, but many improvements are required. The modifications we have introduced are not sufficient. The use of a tolerance value to control prompt γ yield is just a palliative. On the one hand, the only available data are prompt γ detection yield. It is hard to provide a nuclear model validation from those data sets. On the other hand, prompt γ are produced during fragment deexcitation. But we can not check if the primary fragment distributions are correctly predicted by the simulation code. Obviously, we have to work on the nuclear collision models.

Finally, we are able to correctly reproduce some existing experimental data. This point is paving the way of accurate simulations to the design of an *in beam TOF PET* dedicated to the hadrontherapy treatment.

Bibliography

- J.P Bondorf, A.S. Botvina, A.S. Iljinov, I.N. Mushustin, K. Sneppen, and R. Donangelo. Statistical simulation of the break-up of highly excited nuclei. *Nuclear Physics*, A475: 663–686, 1987.
- J.P Bondorf, A.S. Botvina, A.S. Iljinov, I.N. Mushustin, and K. Sneppen. Statistical multifragmentation of nuclei. *Physics Report*, 257:133–221, 1995.
- T.T. Böhlen, F. Cerutti, M. Dosanjh, A. Ferrari, I. Gudowska, A. Mairani, and J.M. Quesada. Benchmarking nuclear models of fluka and geant4 for carbon ion therapy. *Phys. Med. Biol.*, 55:5833–5847, 2010.
- Paulo Alexandre Vieira Crespo. *Optimization of In-Beam Positron Emission Tomography for Monitoring Heavy Ion Tumor Therapy*. PhD thesis, Vom Fachbereich Physik der Technischen Universität Darmstadt, 2005.
- F. Le Foulher, M.Bajard, D.Dauvergne, N.Freud, P.Henriquet, S.Karkar, J.M.Létang, R.Plescak, C.Ray, D.Schardt, E.Testa, M.Testa, and L.Lestand. Monte carlo simulations of prompt γ emission during carbon ion irradiation. *IEEE TNS*, 57, 2010.
- Ch Hartnack, R K Puri, J Aichelin, J Konopka, SA Bass, H Stöcker, and W Greiner. Modelling the many-body dynamics of heavy ion collisions : Present status and future perspective. *The European Physical Journal A*, 1:151–169, 1998.
- A. S. Iljinov, M. V. Mebel, N. Bianchi, E. De SanctisCorresponding, C. Guaraldo, V. Lucherini, V. Muccifora, E. Polli, A. R. Reolon, and P. Rossi. Phenomenological statistical analysis of level densities decay of lifetimes of excited nuclei. *Nuclear Physics A*, 543:517–557, 1992.
- I.Pshenichnov, I.Mishustin, and W.Greiner¹. Distributions of positron-emitting nuclei in proton and carbon-ion therapy with geant4. *Phys.Med.Biol.*, 51:6099–6112, 2006.

- I.Pshenichnov, A.Botvinaa, I.Mishustina, and W.Greiner. Nuclear fragmentation reactions in extended media studied with geant4 toolkit, 2009. URL <http://arxiv.org/pdf/0911.2017>.
- D. Kinet J. Cugnon and J. Vandermeulen. Pion production in central high energy nuclear collisions. *Nuclear Physics*, A379:553, 1982.
- J.Aichelin. The quantum molecular dynamics approach. *Prog.Part.Phys*, 30:191–218, 1993.
- J.Aichelin. Quantum molecular dynamics a dynamical microscopic n-body approach to investigate fragment formation and the nuclear equation of state in heavy ion collisions. *Physics Report (Review Section of Physics Letters)*, 5:233–360, 1991.
- J.Allison, Amako K., Apostolakis J., Araujo H., Dubois P.A., Asai M., Barrand G., Capra R., Chauvie S., Chytraccek R., Cirrone G.A.P., Cooperman G., Cosmo G., Cuttone G., Daquino G.G., Donszelmann M., Dressel M., Folger G., Foppiano F., Generowicz J., Grichine V., Guatelli S., Gumplinger P., Heikkinen A., Hrivnacova I., Howard A., Incerti S., Ivanchenko V., Johnson T., Jones F., Koi T., Kokoulin R., Kossov M., Kurashige H., Lara V., Larsson S., Lei F., Link O., Longo F., Maire M., Mantero A., Mascialino B, McLaren I., Lorenzo P.M., Minamimoto K., Murakami K., Nieminen P., Pandola L., Parlati S., Peralta L., Perl J., Pfeiffer A., Pia M.G., Ribon A., Rodrigues P., Russo G., Sadilov S., Santin G., Sasaki T., Smith D., Starkov N., Tanaka S., Tcherniaev E., Tome B., Trindade A., Truscott P., Urban L., Verderi M., Walkden A., Wellisch J.P., Williams D.C.and Wright D., and Yoshida H. Geant4 developments and applications. *IEEE TNS*, 53 Issue 1:270–278, 2006.
- J.Sulkimoah, M.Takahataay, S.Tanakabg, E.Tcherniaeva, E.Safai Tehranig, M.Tropeanoae, P.Truscottbe, H.Unoaw, L.Urbanv, P.Urbanaq, M.Verderiap, A.Walkdenas, W.Wanderav, H.Weberaf, J.P.Wellischa, T.Wenaus, D. C.Williamsj, D.Wrightg, T.Yamadaaw, H.Yoshidaaw, and D.Zschiesche. Geant4—a simulation toolkit. *Nuclear Instruments and Methods in Physics Research*, A 506:250–303, 2003.
- H. Machner. Pre-equilibrium decay into complex particle channles analysys of double differential cross sections. *Physics Letters B*, 86, 1979.
- Katia Parodi. *On the feasibility of dose quantification with in-beam PET data in radiotherapy with ^{12}C and proton beams*. PhD thesis, Fakultät Matematik und Naturwissenschaften der Technischen Universität Dresden, 2005.
- A. Polanski. Development of methods for simulation of electronuclear process. *Progress in High-Energy Physics and Nuclear Safety*, pages 319–332, 2009.

- Marlen Priegnitz, Fine Fiedler, Daniela Kunath, Kristin Laube, Katia Parodi, Florian Sommerer, and Wolfgang Enghardt. A novel approach for predicting the positron emitter distributions produced during therapeutic ion irradiation. *IEEE Nuclear Science Symposium Conference Record*, 2008.
- W. Shen, B. Wang, J. Feng, W. Zhan, Y. Zhu, and E. Feng. Total reaction cross section for heavy-ion collisions and its relation to the neutron excess degree of freedom. *Nuc. Phys. A*, 491:130–146, Jan 1986.
- E. Testa, M. Bajard, M. Chevalier, D. Dauvergne, F. Le Foulher, N. Freud, J.-M. Letang, J.-C. Poizat, C. Ray, and M. Testa. Monitoring the bragg peak location of 73 mev/u carbon ions by means of prompt γ -ray measurements. *Applied Physics letters*, 93, 2008.
- E. Testa, M. Bajard, M. Chevalier, D. Dauvergne, F. Le Foulher, N. Freud, J.-M. Letang, J.-C. Poizat, C. Ray, and M. Testa. Dose profile monitoring with carbon ions by means of prompt-gamma measurements. *Nuclear Instruments and Methods in Physics Research B*, 267:993–996, 2009.
- V. F. Weisskopf and D. H. Ewing. On the yield of nuclear reactions with heavy elements. *Phys. Rev.*, 57(6):472–485, 1940.
- G. D. Westfall, Z. M. Koenig, B. V. Jacak, L. H. Harwood, G. M. Crawley, M. W. Curtin, C. K. Gelbke, B. Hasselquist, W. G. Lynch, A. D. Panagiotou, D. K. Scott, H. Stöcker, and M. B. Tsang. Light particle spectra from 35 mev/nucleon ^{12}C -induced reactions on ^{197}Au . *Phys. Rev. C*, 29(3):861–863, Mar 1984. doi: 10.1103/PhysRevC.29.861.
- R.R Wilson. Radiological use of fast protons. *Radiol.*, 47:487, 1946.